nature communications

Article

https://doi.org/10.1038/s41467-025-65358-y

Stress changes the material state of a bacterial biomolecular condensate and shifts its function from mRNA decay to storage

Received: 6 September 2025

Accepted: 8 October 2025

Published online: 14 November 2025

Check for updates

Luis A. Ortiz-Rodríguez[1], Hadi Yassine[2,3], Ali Hatami[4], Vidhyadhar Nandana[2], Christopher A. Azaldegui[5], Jiayu Cheng[1], Yingxi Zhu[4], Jared M. Schrader[2,3] ✉ & Julie S. Biteen[1,5] ✉

Bacterial ribonucleoprotein bodies (BR-bodies) are dynamic biomolecular condensates that play a pivotal role in RNA metabolism. We investigated how BR-bodies significantly influence mRNA fate by transitioning between liquid- and solid-like states in response to stress. With a combination of single-molecule and bulk fluorescence microscopy, biochemical assays, and quantitative analyses, we determine that BR-bodies promote efficient mRNA decay in a liquid-like condensate during exponential growth. On the other hand, BR-bodies are repurposed from sites of mRNA decay to reservoirs for mRNA storage under stress; a functional change that is enabled by their transition to a more rigid state, marked by reduced internal dynamics, increased molecular density, and prolonged residence time of Ribonuclease E. Furthermore, we manipulated ATP levels and translation rates, and we conclude that the accumulation of ribosome-depleted mRNA is a key factor driving BR-body rigification, and that condensate maturation further contributes to this process. Upon nutrient replenishment, stationary-phase BR-bodies disassemble, releasing stored mRNAs for rapid translation, demonstrating that BR-body function is governed by a reversible mechanism for resource management. These findings reveal adaptive strategies by which bacteria regulate RNA metabolism through condensate-mediated control of mRNA decay and storage.

Biomolecular condensates are dynamic macromolecular assemblies that often form via phase separation[1,2], a reversible process that enables the cell to respond rapidly to environmental changes[3]. These assemblies are selectively permeable and can exchange client molecules[1,4]. Depending on their physical state, which can range from liquid droplets to hydrogels and insoluble aggregates, condensates facilitate various biological functions[1,5]. Liquid-like condensates promote biochemical reactions by allowing internal diffusion and exchange with the dilute phase, while gel- and solid-like condensates have reduced diffusion and exchange, which slow down biochemical reactions and may potentially sequester biomolecules for storage[1,2]. Notably, transitions from the liquid to solid state in biomolecular condensates have been linked to neurodegenerative protein aggregation disorders[6,7]: reducing the fluidity of these condensates can negatively affect their function[8,9]. However, in other cases, such as germ granules, solid-like states play

[1]Department of Chemistry, University of Michigan, Ann Arbor, MI, USA. [2]Departments of Chemistry and Biological Sciences, Wayne State University, Detroit, MI, USA. [3]Department of Biology, Indiana University, Bloomington, IN, USA. [4]Department of Chemical Engineering and Materials Science, Wayne State University, Detroit, MI, USA. [5]Doctoral Program in Chemical Biology, University of Michigan, Ann Arbor, MI, USA. ✉e-mail: jaschrad@iu.edu; jsbiteen@umich.edu

important roles in mRNA storage and translational control in the developing embryo[10].

Recently, biomolecular condensates have emerged as a broadly utilized mechanism for organizing diverse biochemical pathways within the bacterial cytoplasm[11–19], and this organizational paradigm is particularly important in bacteria because these organisms generally lack membrane-bound organelles[20,21]. Bacterial ribonucleoprotein bodies (BR-bodies), the organelles that contain the RNA degradation machinery, were the first bacterial condensates demonstrated to assemble via liquid-liquid phase separation (LLPS), driven by interactions between the large intrinsically disordered region (IDR) of ribonuclease E (RNE; Fig. 1a) and RNA[11].

Caulobacter crescentus BR-bodies share functional similarities with eukaryotic processing bodies (P-bodies) and stress granules (SGs), as all three contain the mRNA decay machinery. RNE (Fig. 1a), the core scaffold and driver of BR-body function, is the essential and rate-limiting factor in bacterial mRNA decay[22,23]. Similarly, Xrn1 is a core component of eukaryotic P-bodies and SGs, and it controls cytoplasmic mRNA decay[24–26]. In addition, similar types of molecules are enriched in BR-bodies (Fig. 1b, c), P-bodies, and SGs, including DEAD-box RNA helicases, Lsm proteins, miRNAs, small RNAs, and translationally repressed mRNAs[27]. P-bodies and SGs have been predominantly studied under conditions of cell stress, and some studies indicate that P-bodies promote mRNA decay, while others show an mRNA storage function, whereas SGs have only been found to promote storage[11,25,28]. These differences in the decay and storage functions are correlated with differences in the mobility of molecules within P-bodies[25,28–31] and SGs[32–34], since P-bodies have been found to have higher mobility and more rapid exchange with the dilute phase than SGs. BR-bodies have been predominantly studied in exponentially growing bacterial cells, during which they appear to have liquid-like properties that promote mRNA decay (Fig. 1c)[11,35]. In contrast, under cell stress, BR-bodies undergo increased condensation that correlates with enhanced survival under these conditions, yet their internal dynamics and rates of mRNA degradation have not been previously explored under stress[11]. Evidence from multiple bacterial species has shown that mRNA decay rates are reduced under conditions of nutrient limitation, such as when cells enter stationary phase, yet the role of BR-bodies in this slowdown of mRNA decay has not yet been explored[36–41].

In this study, we investigate changes in the dynamics within BR-bodies between exponential growth and the stationary phase and how these differences impact the mRNA decay pathway. We define the material state of a biomolecular condensate as the set of physical properties that determine internal mobility, exchange with the surrounding environment, condensate compaction, and thus biological function. Furthermore, in this work, a condensate is considered liquid-like when it exhibits dynamic internal rearrangement, rapid molecular exchange with the surrounding environment, lower biomolecular density, and short residence times of key components, while rigid condensates show reduced internal molecular diffusion, longer component residence times, increased compaction, and reduced exchange with the surrounding environment. Our live-cell single-molecule microscopy results demonstrate that BR-bodies transition from a dynamic, liquid-like state during exponential growth to a less dynamic, more rigid material state during stress. We demonstrate that this transition is associated with a functional shift from enhancing mRNA decay in the exponential phase to promoting mRNA storage in the rigid state. In line with these results, we measure that the in vitro maturation of RNE condensates and subsequent arrest of dynamics lead to a strong reduction in RNE activity. Given the similarities between BR-bodies and eukaryotic biomolecular condensates like SGs and P-bodies, our findings further suggest that differences in cell growth conditions may also alter the material properties of P-bodies and SGs to shift the inherent preferences for mRNA decay vs. storage across diverse organisms.

Results

The transition from exponential to stationary phase is associated with BR-body rigidification

To investigate the dynamics of molecules within BR-bodies and their response to stress, we labeled the endogenous copy of RNE with the green-to-red photoconvertible fluorescent protein mEos3.2 (RNE-mEos3.2; Fig. 1d)[42]. This labeling strategy allows us to study the properties of BR-bodies as a whole using bulk fluorescence in the initial mEos3.2 green state, and to measure their internal dynamics at the single-molecule level in the mEos3.2 red state after photoconversion using 405-nm excitation. We compared BR-body dynamics during exponential and stationary growth phases to understand the effect of non-invasively induced cellular starvation, ensuring physiologically relevant observations of the stress response. We further sought to resolve two previous confounding observations: (1) there is an increased number of BR-bodies and a higher copy number of RNE in each condensate in cells at the stationary phase (Supplementary Fig. 1a)[11], a nutrient-deprived state during which bacterial growth and division cease, and yet (2) mRNA decay is slower in the stationary phase.

To investigate how the stationary phase alters BR-bodies, we performed time-lapse imaging of cells in exponential and stationary phases. In the exponential phase, BR-bodies rapidly assemble and disassemble, consistent with their known role in mRNA decay (Fig. 1d, Supplementary Movie 1). However, in the stationary phase, BR-bodies are dramatically stabilized (450-fold; Fig. 1d, Supplementary Movie 2). As RNA is required for BR-body phase separation[11], the decreased dissolution rate of BR-bodies during the stationary phase suggests reduced RNA decay activity, as mRNA degradation is necessary for BR-body disassembly (Fig. 1c)[11]. Single-molecule tracking of RNE-mEos3.2 and the degradosome protein aconitase-PAmChy, previously identified as a direct binding partner to RNE[11,43,44] and core component of the *C. crescentus* RNA degradosome, revealed measurably reduced diffusivity of RNE and its degradosome client proteins within BR-bodies during the stationary phase (Fig. 1e and Supplementary Fig. 1b, c), consistent with a more rigid internal microenvironment. In addition, we compared RNE-mEos3.2 diffusion in both growth phases with the apparent diffusion of immobile RNE-mEos3.2 molecules in fixed cells. While we measured slow diffusion of RNE-mEos3.2 within BR-bodies during the exponential phase, this value is higher than our lower bound as determined in fixed cells. In contrast, the diffusion profile of RNE-mEos3.2 in stationary phase cells closely matches that of fixed cells, suggesting that, under our experimental conditions, RNE-mEos3.2 is essentially static within the BR-bodies during the stationary phase. Furthermore, the residence time of RNE within BR-bodies is 370-fold longer in the stationary phase compared to the exponential phase (Fig. 1f). After identifying the RNE-mEos3.2 clusters with a density-based cluster analysis[45], we determined the molecular density and estimated the BR-body diameter, $\bar{d}$, as the maximum span of each cluster (Fig. 1g,h). In the exponential phase, the BR-bodies are less dense and larger ($\bar{d} = 206 \pm 2$ nm) than in the stationary phase ($\bar{d} = 102 \pm 1$ nm) (mean ± SEM; $p < 0.001$). Importantly, the decreased diffusivity and increased residence time of RNE within the BR-bodies, along with their compaction, are also observed under ethanol stress, indicating that dynamic arrest behavior likely occurs under other inducing stresses (Supplementary Figs. 1d–f, 2). This compaction explains the decreased internal dynamics, where the rigid state constrains RNE within the BR-body.

We also analyzed the diffusion of RNE outside the BR-bodies in both exponential and stationary phase cells to determine whether the observed changes in RNE mobility were specific to the condensate internal microenvironment. The mobility of RNE molecules not associated with the BR-bodies remained unchanged between growth phases (Supplementary Fig. 1c), indicating that the reduced mobility observed within BR-bodies during stationary phases arises

https://doi.org/10.1038/s41467-025-65358-y

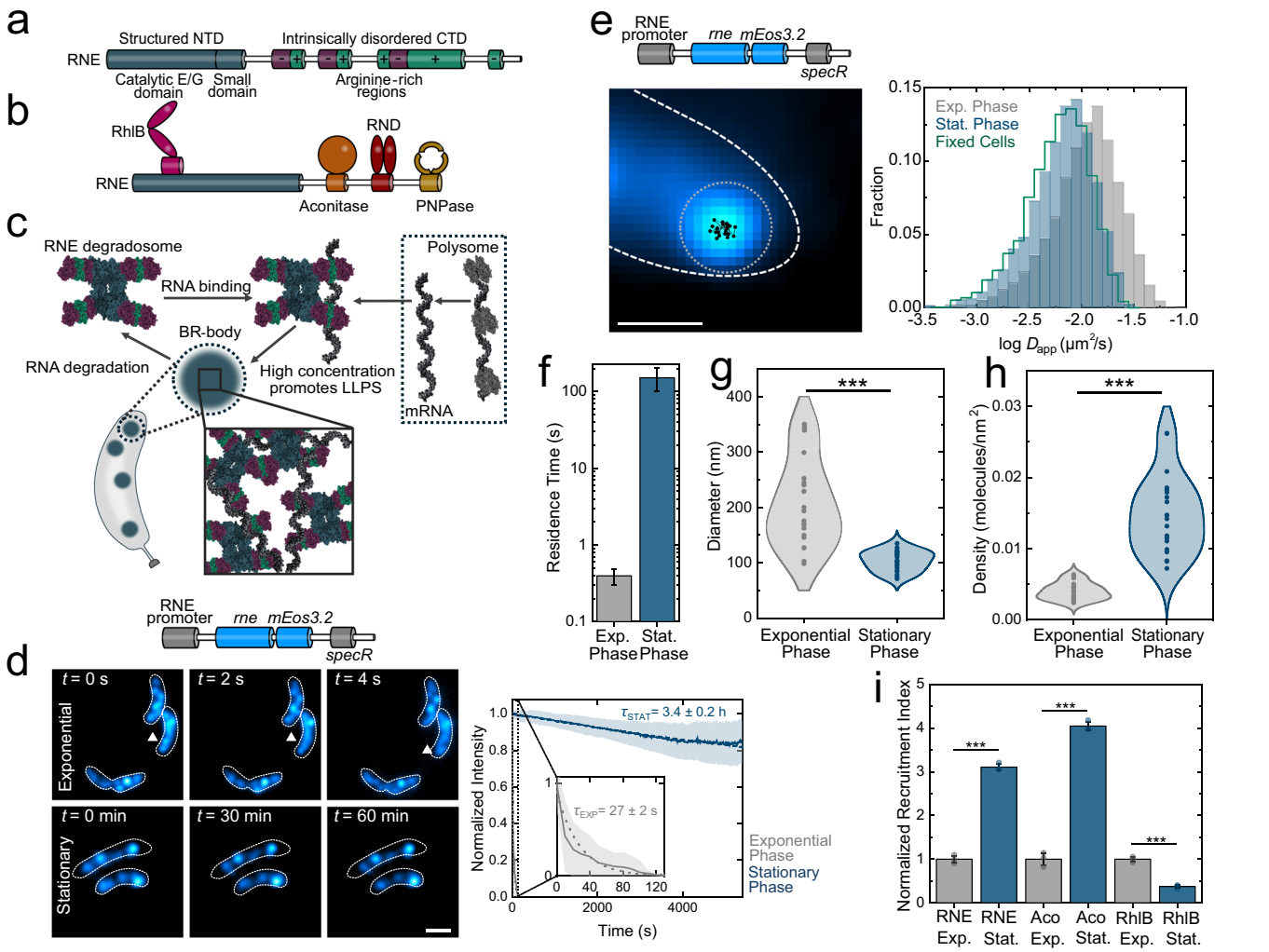

Fig. 1 | BR-bodies are dynamically arrested and compacted upon entering the stationary phase. a Domain organization of *C. crescentus* RNase E (RNE). **b** The *C. crescentus* RNA degradosome. **c** Working model: untranslated mRNAs and the degradosome phase separate into BR-bodies, which concentrate decay factors to accelerate degradation; condensates dissolve as mRNA is degraded. **d** Lifespans of condensates imaged with RNE-mEos3.2. Top: construct schematic. Middle: representative cells (white outlines) showing RNE-mEos3.2 (blue) foci (arrowheads). Scale bar: 500 nm. Bottom: decay profiles of photobleaching-corrected intensities. Lines indicate the mean, and shaded regions indicate the standard deviation, with lifespans (τ_{EXP}, τ_{STAT}). $N = 427$ foci (211 cells, exponential) and $N = 932$ foci (232 cells, stationary). Similar results were obtained from three independent colony replicates. **e** Single-molecule tracking of RNE-mEos3.2 inside BR-bodies. Left: representative trajectory (black dots, 20-ms frames) within a BR-body (dotted circle). Scale bar: 500 nm. Right: apparent diffusion coefficients in exponential and stationary phases, compared to fixed control. Trajectories analyzed: 5001 (exponential), 6347 (stationary). **f** Residence times of RNE-mEos3.2 from exponential fits of decay curves combining $n = 3$ replicates per delay. Error bars: propagated fitting errors (derived parameters). **g** BR-body diameter estimated from the maximum cluster. $n = 20$ clusters per condition. Two-tailed Welch's t-test, $p = 1.34 \times 10^{-5}$. **h** Density of RNE-mEos3.2 localizations within BR-bodies. $n = 20$ clusters per condition. Two-tailed Welch's t-test, $p = 2.92 \times 10^{-8}$. **i** Normalized recruitment index (NRI) of RhlB-PAmChy, Aco-PAmChy, and RNE-mEos3.2 in the stationary and exponential phase, showing incomplete degradosomes. Dots indicate the replicates ($n = 3$). Error bars indicate propagated standard deviations. All values are normalized to the mean NRI of the exponential phase, setting the exponential phase values to 1. The error for each condition was calculated by propagating the original standard deviation using standard error propagation rules. Two-tailed Welch's t-test, $p = 1.11 \times 10^{-5}$ (RNE), 3.38×10^{-5} (aconitase), 3.38×10^{-4} (RhlB). *** in (**g**) and (**i**) denotes $p < 0.001$.

from changes in the condensate internal microenvironment rather than reflecting overall cellular changes between growth phases. This lack of a change in diffusion outside the BR-bodies reflects the short timescales probed by our single-molecule trajectories (~160 ms), which primarily report on local motions and therefore do not capture slower cytoplasmic dynamics[46]. In contrast, the microenvironment within stationary phase BR-bodies is sufficiently dense that a measurable reduction in RNE-mEos3.2 mobility is evident even on these short timescales, while condensate-level diffusion becomes distinct at longer observation windows (Supplementary Fig. 3).

To determine whether BR-bodies retain characteristics of phase-separated condensates during the stationary phase, rather than forming irreversible aggregates, we treated cells with 5% 1,6-hexanediol (HD), a commonly used aliphatic alcohol that disrupts the weak hydrophobic interactions essential for phase separation[47–49]. BR-bodies dissolve within ~25 min of HD treatment (Supplementary Fig. 1g), confirming that they remain sensitive to HD despite rigidification during the stationary phase. This finding suggests that BR-bodies retain hallmark features of biomolecular condensates, even in the rigid state, and that the observed rigidification reflects a dynamic arrest rather than a transition to an aggregated or misfolded state.

BR-bodies concentrate the RNA degradosome complex, which in *C. crescentus* contains aconitase, RhlB, and PNPase (Fig. 1b)[11,44]. We quantified the recruitment of aconitase and RhlB to BR-bodies during exponential and stationary phases, normalizing by differences in

overall expression levels. After normalization, we found that aconitase recruitment increases 4-fold, while RhlB recruitment decreases 3-fold in the stationary phase (Fig. 1i). These results reveal a stoichiometric reorganization of BR-bodies under stress. In particular, the concomitant loss of RhlB and enrichment of RNE and aconitase indicate the presence of incomplete degradosomes inside BR-bodies during the stationary phase. DEAD-box RNA helicases are central regulators of biomolecular condensates[50]; their ATPase cycle maintains the condensates in a dynamic, non-equilibrium state, facilitating the enrichment of client molecules and buffering the dispersed ribonucleoprotein pool. The decreased recruitment of the DEAD-box RNA helicase RhlB thus likely impairs the internal remodeling of BR-bodies, potentially contributing to their rigidification during stress.

Increased levels of poorly translated mRNA and maturation trigger the transition to the rigid material state

During the stationary phase, bacterial cells encounter nutrient scarcity, which slows down cellular processes, including metabolic activity, leading to lower ATP levels (Fig. 2a)[51]. Reduced ATP levels subsequently impact various processes, including protein synthesis and translation, promote phase separation of proteins with intrinsically disordered regions (IDRs)[18], contribute to protein aggregation[12,13], and cause physical changes in cytoplasm[46,52], creating a glassy state that slows the diffusion of mesoscale objects such as BR-bodies (Supplementary Fig. 3). Additionally, since DEAD-box helicases like RhlB require ATP hydrolysis to remodel, dissolve, cooperatively bind RNA[53], prevent strong interactions, and maintain the fluidity of the condensates[50], the low ATP levels at stationary phase may impair these activities.

To separate the effects of low ATP levels and reduced translation on BR-body rigidification, we artificially decreased ATP and translation levels in exponential phase cultures of *C. crescentus*. To lower ATP levels, we treated the cultures with the protonophore carbonyl cyanide *m*-chlorophenyl hydrazone (CCCP) to disrupt the proton motive force[54], rapidly inhibiting ATP synthase. A 20-min treatment with 100 µM CCCP was found to reduce cellular ATP concentrations to levels comparable to those observed during the stationary phase (Fig. 2a). To reduce translation levels, we used puromycin (150 µg/mL for 30 min), which prematurely cleaves peptide chains[55] and releases ribosome subunits and mRNA, thereby increasing the availability of ribosome-depleted transcripts in the cytoplasm. Since puromycin treatment also results in ATP levels similar to those observed in the stationary phase (Fig. 2a), we treated cells with CCCP and the translation elongation inhibitor chloramphenicol as a control. Chloramphenicol prevents translation by blocking peptide bond formation and accumulating ribosomes on mRNA[56]. Interestingly, treating exponential phase cultures with CCCP and puromycin leads to long-lived BR-bodies (Fig. 2b), similar to those observed during stationary phase (Fig. 1d). However, when cells are treated with the combination of CCCP and chloramphenicol, BR-bodies remain short-lived, similar to those observed during exponential phase in the absence of stress (Fig. 2b). Similarly, BR-bodies remain short-lived when cells are treated with chloramphenicol only (Supplementary Fig. 4). This finding suggests that the increased lifespan of BR-bodies upon treatment with CCCP might be an indirect effect of dropping ATP levels inhibiting translation rather than directly related to ATP availability. Translation is typically the most energy-intensive process during exponential growth[57,58], and ATP and GTP are essential for several steps in translation, including the esterification of amino acids to tRNAs, selection of the aa-tRNAs to the ribosome, the assembly of ribosomal subunits, and the translocation of ribosomes along the mRNA. When NTP levels are decreased, these processes slow, resulting in reduced translation rates. Additionally, biorthogonal non-canonical amino acid tagging (BONCAT) revealed a significant decrease in translation levels during the late stationary phase, with reductions of 30-fold, as well as in cells treated with puromycin, CCCP, and the combination of CCCP and chloramphenicol, all relative to the exponential phase (Fig. 2c, Supplementary Fig. 5).

Similar to the extended lifespan of BR-bodies observed upon treatment with CCCP and puromycin, these treatments also replicated stationary-phase decreases in RNE-mEos3.2 diffusivity inside the BR-bodies (Fig. 2d, Supplementary Fig. 6a), BR-body size (Fig. 2e, Supplementary Fig. 6b), RNE molecular density (Fig. 2f, Supplementary Fig. 6c), BR-body number (Supplementary Fig. 7), and residence time within BR-bodies (Supplementary Fig. 3). Conversely, cells treated with a combination of CCCP and chloramphenicol do not rigidify. This finding suggests that the rigid material state transition in the stationary phase requires increased amounts of ribosome-free mRNA transcripts in the cytoplasm, whereas ATP scarcity alone is insufficient.

We identified low ribosome occupancy as a key factor contributing to the rigid material state of BR-bodies during the stationary phase. However, under prolonged stress, biomolecular condensates have been observed to mature from having liquid-like to solid-like properties[1,59–63]. Initially, their components interact transiently: molecules freely rearrange and exchange with the surrounding phase, resembling liquid behavior. Over time, mechanisms such as entanglement of disordered polypeptides[64], vitrification[65], percolation[66], and nucleation and elongation of amyloid-like fibers[67] contribute to rigidification and decreased molecular dynamics[68]. We investigated the role of maturation in BR-body rigidification by in vivo fluorescence recovery after photobleaching (FRAP) of BR-bodies (RNE-mEos3.2) in cultures of *C. crescentus* cells at 6 h and 24 h into the stationary phase (Fig. 2g, h). The condensates become less dynamic over time in the stationary phase. The BR-body fluorescence recovers only minimally at both time points, consistent with a rigid material state, but BR-bodies are slightly more dynamic at 6 h than at 24 h. To further investigate the role of maturation, we reconstituted the system in vitro and extracted meaningful information based on RNE, the first bacterial protein found to undergo LLPS at physiological concentrations without crowding agents[11]. FRAP performed on RNE droplets reconstituted in vitro and aged with RNA for 30 min, 4 h, and 8 h (Supplementary Fig. 8) revealed that condensates aged for 30 min were significantly more dynamic, with nearly full fluorescence recovery within 2.5 min, whereas condensates aged for 4 h exhibited minimal recovery, and 8 h were even less dynamic. These results support the role of maturation in changing the material state of BR-bodies.

The material state transition of BR-bodies during stress shifts their function from promoting mRNA decay to facilitating mRNA storage

Our in vivo and in vitro results establish that, during stress conditions, the internal dynamics and structure of BR-bodies become more rigid. Previous two-color images of mRNA and RNE using MS2 RNA labeling[69] and fluorescence in situ hybridization (FISH) during exponential growth have shown that transcripts such as *rsaA* exhibit low colocalization (~28%) with RNE in BR-bodies in conditions allowing active RNA degradation[35]. However, colocalization increases significantly (~80%) when RNE endonuclease cleavage is blocked using an RNE active site mutation (ASM) involving the two residues coordinating the catalytic Mg^{2+} ion in the active site[35]. These results suggest that the transition to a more rigid material state, along with its associated effects, may enable BR-bodies to store mRNA during stress conditions.

To investigate the role of BR-bodies in mRNA storage, we performed two-color imaging of RNE and mRNA using a live-cell MS2 system and FISH, and we measured mRNA degradation rates using quantitative reverse transcription polymerase chain reaction (qRT-PCR). Notably, this study employs an MS2 system optimized to

https://doi.org/10.1038/s41467-025-65358-y

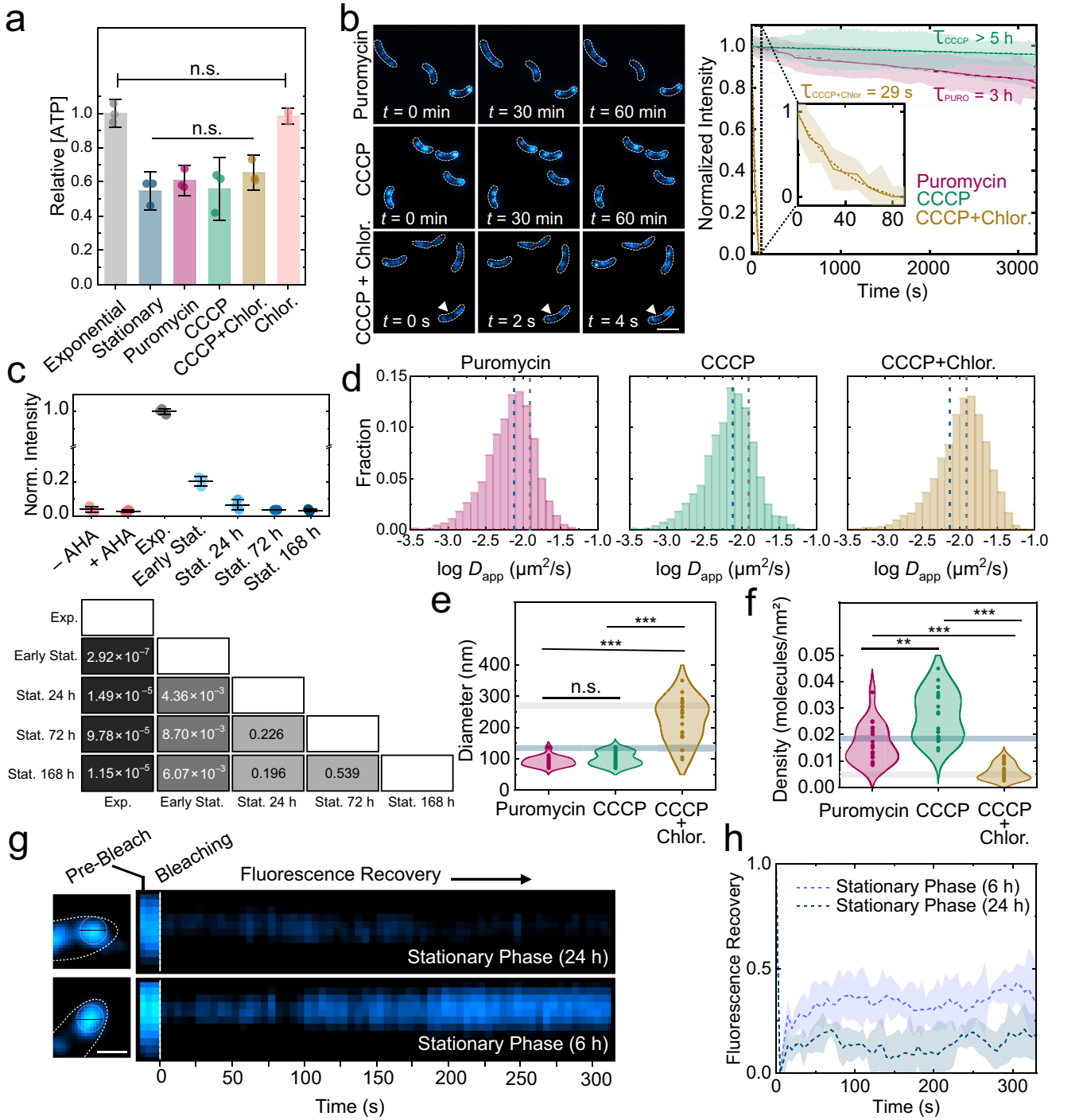

Fig. 2 | Rigidification of BR-bodies is promoted by increased levels of poorly translated mRNAs. a Intracellular ATP in *C. crescentus* measured with a luciferase assay after treatment. Levels normalized to the exponential phase. Dots: replicates ($n = 3$). Error bars: SD. Two-tailed Welch's *t*-test: $p = 1.49 \times 10^{-3}$ (stationary), 1.14×10^{-3} (puromycin), 1.29×10^{-2} (CCCP), 2.71×10^{-3} (CCCP+chloramphenicol), and 0.695 (chloramphenicol). **b** Lifespans of BR-bodies in treated cells. Left: representative images of RNE-mEos3.2 (blue) in cells (white outlines) as a function of treatment and time, *t*; arrowheads mark foci. Scale bar: 2 μm. Right: photobleaching-corrected decay profiles. $N = 308$, 347, 241 foci from 88, 193, 301 cells for puromycin, CCCP, and CCCP+chloramphenicol, respectively. Lines: mean; shaded regions: SD. Similar results were obtained from three independent colony replicates. **c** Top: relative translational levels in exponential and stationary phases by BONCAT, with AHA and chloramphenicol controls. Scatter-interval plot, $n = 3$. Central line: mean; bounds: ±1 SD. Bottom: two-tailed Welch's *t*-test *p* values. **d** Apparent diffusion coefficients of RNE-mEos3.2 trajectories. Dashed lines: medians. Trajectories: 2126 (puromycin), 1637 (CCCP), 1441 (CCCP+chloramphenicol). **e** BR-body diameters. Lines: mean for exponential vs stationary. $n = 20$ clusters per condition. Two-tailed Welch's *t*-test: $p = 0.157$ (puromycin vs. CCCP), 5.45×10^{-8} (puromycin vs. CCCP+chloramphenicol), 1.35×10^{-7} (CCCP vs. CCCP+chloramphenicol). **f** Density of RNE-mEos3.2 localizations. Lines: mean for exponential vs. stationary. $n = 20$ clusters per condition. Two-tailed Welch's *t*-test: $p = 1.83 \times 10^{-4}$ (puromycin vs. CCCP), 2.64×10^{-6} (puromycin vs CCCP+chloramphenicol), 9.36×10^{-10} (CCCP vs. CCCP+chloramphenicol). **g** Dynamics during prolonged stationary phase. FRAP kymographs at 6 h and 24 h showing RNE-mEos3.2 foci bleaching and recovery. Scale bar: 500 nm. **h** FRAP of RNE-mEos3.2 in early vs. late stationary phase. $N = 20$ foci. Line: mean; shaded region: SD. Statistics in (**a**, **e**, **f**): $^{***}p < 0.001$, $^{**}p < 0.005$, n.s. $p > 0.05$.

accurately track short-lived mRNAs[70]. We selected four key mRNA transcripts needed for *C. crescentus* exponential growth: *rsaA*, *rne*, *spmX*, and *ctrA*. All four mRNAs were previously found to be stabilized in an RNE-IDR truncation mutant incapable of making BR-bodies, suggesting BR-bodies play a role in their degradation[35,71]. The RsaA S-layer protein is the most abundant protein in *C. crescentus*[72]. RsaA was chosen for comparison with the prior result, where RNE cleavage is blocked using the ASM, providing insight into the role of the catalytic activity of RNE in the condensate and its effect on transcript recruitment into BR-bodies[35]. RNE is crucial in RNA processing, degradation[22,23], BR-body formation, and cell fitness[11]. The integral membrane protein SpmX enables cell division by localizing the histidine kinase DivJ to the stalked pole[73,74]. Finally, CtrA is a master regulator of the cell cycle; it controls chromosome replication and transcription, and it modulates the expression of about 25% of cell cycle-regulated genes in *C. crescentus*[75–79]. These strategically selected transcripts enabled us to thoroughly assess the role of BR-bodies in mRNA storage under stress and to determine the relevance of the stored transcripts.

Images of MS2-labeled *ctrA*, *spmX*, and *rsaA* transcripts (Fig. 3a,b, and Supplementary Fig. 9) highlight their higher recruitment to BR-bodies during the stationary phase compared to the exponential phase; these datasets were quantified using Pearson correlation coefficients (PCC). All transcripts colocalize more with BR-bodies during the stationary phase, similar to the behavior of *rsaA* when RNE cleavage is blocked, suggesting significantly lower degradation activity by RNE during this phase. This mRNA RNE colocalization is further confirmed by FISH (Supplementary Fig. 10). To ensure that the observed differences in BR-body colocalization across growth phases reflect transcript-specific recruitment dynamics rather than analytical artifacts or changes in overall transcript abundance, we used transfer-messenger mRNA (tmRNA) as a negative control. tmRNA is abundant in *C. crescentus*, and is strongly depleted from the BR-bodies with a $\log_2$ fold-change of −2.8[35]. Upon applying the same colocalization analysis to the target transcripts, we found that tmRNA colocalizes significantly less with BR-bodies (PCC = 0.13 ± 0.04) compared to all other transcripts, even during exponential phase (Supplementary Fig. 11). These results confirm that the high levels of colocalization observed for specific transcripts during stationary phase are not simply due to increased transcript abundance; rather, they reflect selective recruitment into BR-bodies under stress.

We also assessed the stability of these transcripts tagged with MS2-RNA hairpins by analyzing the photobleaching-corrected intensities of MS2-mChy foci colocalized with RNE foci during both growth phases (Fig. 3c and Supplementary Fig. 9). To ensure that our observations accurately reflect transcript stabilization and not artifacts of the labeling system, we employed two versions of the MS2 system which are both utilized with a MS2-mChy dimerization deficient variant[80]: a 48×-array with weaker MS2 coat protein RNA hairpin affinity[70] and a 96×-array[35]. Previous studies have demonstrated that binding of the coat protein to MS2 binding sites artifactually stabilizes mRNA[81–83]. Therefore, we confirmed that any observed accumulation of the mChy signal within BR-bodies was due to real transcript stabilization and not an effect of the labeling system. As shown in Fig. 3a,b, mChy foci do not colocalize with BR-bodies during the exponential phase when using the 48×-array system. However, using the 96×-array version (Supplementary Fig. 9), we observed mChy foci colocalizing with BR-bodies, even during the exponential phase. Despite the potential transcript stabilization caused by the more perturbing 96×-array MS2 system, we still observed significant differences in the decay profiles between exponential and stationary phases. During exponential phase, MS2-mChy (96×-array) foci disassemble in under a few min, consistent with rapid internal decay of mRNAs (Supplementary Fig. 9). In contrast, during stationary phase, MS2-mChy (48×-array) foci and stably colocalize with BR-bodies for significantly longer, indicating slowed mRNA decay (Fig. 3c and Supplementary Fig. 9). To investigate the observations of the MS2-tagged RNAs, we measured the RNA decay rates. mRNA half-life measurements by qRT-PCR confirmed this stabilization: *rne*, *spmX*, and *ctrA* exhibit 20-, 65-, and 200-fold stability increases, respectively, from exponential to late stationary phase (Fig. 3d), and the stabilization was confirmed by a second method, mRNA FISH, for *ctrA* mRNA and *spmX* mRNA (Supplementary Fig. 12). To test whether stabilization in stationary phase depends on BR-body formation, we measured the stability of *spmX* and *ctrA* transcripts in stationary phase cultures of *C. crescentus* expressing RNE-ΔCTD; these cells cannot assemble BR-bodies[11]. In this background, transcript stabilization was reduced to only ~3-fold, confirming that BR-bodies are essential for the pronounced stabilization of mRNA during stress (Supplementary Fig. 12). Together, these measurements suggest that the rigid state of RNE is associated with a dramatic slowdown in mRNA decay activity, consistent with a model in which BR-body material state regulates RNA turnover.

Hfq is a well-known regulator of RNA stability, and in *E. coli*, Hfq was observed to form condensates with RNA under conditions of nutrient deprivation, where it was also observed to colocalize with *E. coli* RNE[16,84,85]. In *C. crescentus*, Hfq was observed to colocalize to a subpopulation of BR-bodies[43], suggesting it might impact the stability of transcripts in rigid BR-bodies observed in the stationary phase. To test whether the RNA chaperone Hfq, a BR-body constituent[43], contributes to transcript stabilization, we measured *ctrA* mRNA decay in a *Δhfq* background. In exponentially growing *Δhfq* cells, *ctrA* mRNA decays slightly more slowly than in wild-type cells, but still degrades rapidly (Supplementary Table 1), indicating that Hfq is not required for rapid turnover in the exponential phase. In the stationary phase, *ctrA* mRNA remains highly stable in *Δhfq* cells, similarly to wild type, suggesting that Hfq is not required for BR-body-mediated transcript stabilization. Consistently, the diffusion profile of RNE-mEos3.2 within BR-bodies remains unchanged in the *Δhfq* background (Supplementary Fig. 13), indicating that the change to the rigid material state does not depend on Hfq. Hence, the stabilization during the stationary phase is independent of Hfq and instead reflects protection conferred by the BR-body environment itself. As an additional control, we measured the stability of tmRNA (Supplementary Table 1), a highly abundant transcript that is not enriched in the BR-bodies. tmRNA remained fully stable in both exponential and stationary phases (>8 min and >16 min half-lives, respectively), confirming that transcripts not recruited into BR-bodies do not exhibit phase-dependent changes in decay rate. This finding further supports the model that BR-body-mediated stabilization depends on selective mRNA recruitment.

To investigate whether the reduced RNA cleavage activity of RNE is a direct result of rigidification, we assessed the cutting activity of RNE in 30-min, 4-h, and 8-h in vitro-reconstituted condensates (Fig. 3e). These aged RNE droplets were formed with RNE and RNA, but without Mg^{2+}, an essential cofactor for RNA cleavage by RNE. At each droplet age, RNA cleavage was initiated by adding Mg^{2+}, and samples were collected at various time points to assay RNA cleavage[71]. RNE efficiently cleaves the *rne* 5′ UTR in droplets aged for only 30 min[71], with the corresponding band in the PAGE gel disappearing within 30 min of Mg^{2+} addition (Fig. 3e). In contrast, virtually no RNA cleavage was observed in the rigidified droplets at the 4-h and 8-h timepoints. This finding suggests that maturation into the rigid state can directly shut off RNE cleavage. Furthermore, we hypothesize that BR-body formation during stress serves as a repository for mRNA and a means to sequester RNE and potentially other degradative enzymes in an inactive state. This hypothesis is supported by the higher amount of RNE in condensates during the stationary phase, and by our recent work, where we demonstrated that overexpression of RNA during the exponential phase leads to growth arrest[71]. Taken together with our in vitro results, these results support a model in which BR-body

https://doi.org/10.1038/s41467-025-65358-y

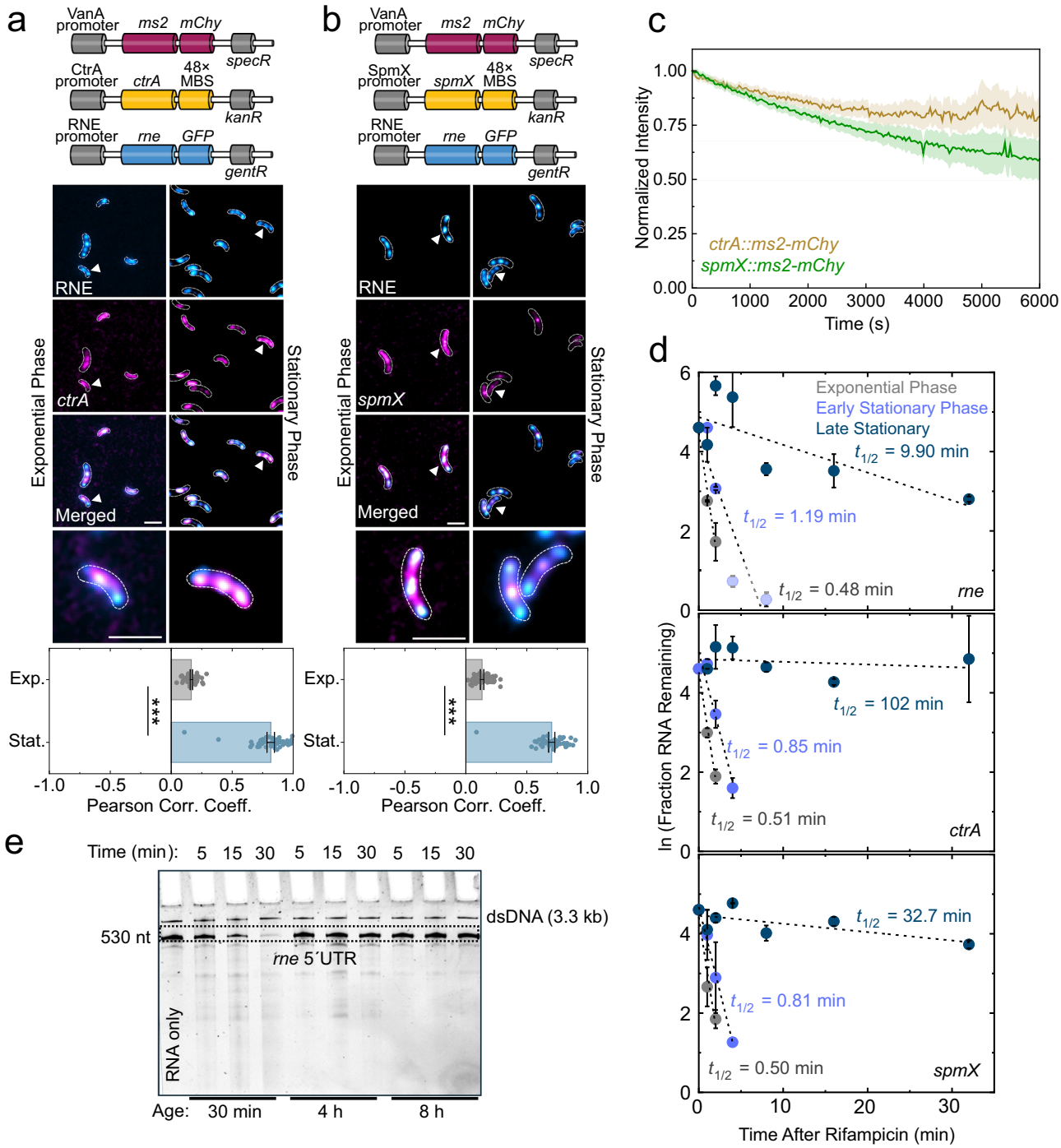

Fig. 3 | Rigidification of BR-bodies switches their function from mRNA decay to storage of key growth mRNAs. Stability of the *ctrA* (**a**) and *spmX* (**b**) transcripts in BR-bodies. Top: genetic constructs used to observe the transcript stability within the BR-bodies in vivo. Middle: Representative two-color images showing higher recruitment of the *ctrA* and *spmX* transcripts (magenta) to BR-bodies (blue) during the stationary phase (left) relative to the exponential phase (right). The merged channel is shown on two magnification levels for clarity. Bottom: Differences in recruitment quantified by the Pearson correlation coefficients between channels. Circles: PCC values for each cell. Error bars: SEM from 50 cells analyzed per phase. *** denotes $p < 0.001$. Arrowheads indicate representative foci. Scale bars in (**a**) and (**b**): 2 μm. Two-tailed Welch's *t*-test, $p = 8.58 \times 10^{-39}$ and 2.19×10^{-44} for *ctrA* and *spmX*, respectively. Similar results were obtained from three independent colony replicates. **c** Decay profiles of *ctrA* and *spmX* in the late stationary growth phase. Analyses include $N = 108$ and 174 foci for the *ctrA* and *spmX* transcripts, respectively, measured across 28 and 49 cells, respectively. Lines indicate the mean intensity decay curves, and shaded regions indicate the standard deviation of the intensity values across all foci analyzed. **d** qRT-PCR measurements of RNA half-lives for *rne*, *ctrA*, and *spmX* transcripts highlight the changes in transcript stability from the exponential phase to the late stationary phase. Error bars: standard deviation from three biological replicates. **e** Condensate aging leads to decreased RNE cutting activity in vitro, as evidenced by the *rne* mRNA band in a 7% urea TBE/PAGE gel. The experiment was repeated three times.

rigidification reduces RNE activity, allowing for selective preservation of mRNAs during stress.

Fluidized BR-bodies are capable of the functional release of mRNAs

Stored mRNAs may be useful for growth-arrested cells either by acting as a nutrient source to promote regrowth or by being released to ribosomes to restart the translation program upon the addition of new nutrients. To determine if mRNA release and subsequent translation can occur after cells exit the stationary phase and enter exponential growth, we assessed whether rigidification is reversible by observing if stationary-state BR-bodies fluidize over time after nutrient replenishment (Supplementary Fig. 14). Indeed, BR-body disassembly was detected after 90 min of nutrient replenishment. We further investigated transcript storage by BR-bodies post-nutrient replenishment by monitoring the colocalization of the *spmX* transcript with BR-bodies in stationary phase cultures (Supplementary Fig. 15). After 3 h, the colocalization profile of *spmX* with BR-bodies returns to that observed during exponential phase (i.e., PCC = 0.22 ± 0.05 vs. 0.25 ± 0.04 in Fig. 3b), suggesting that stored mRNA exits BR-bodies upon removal of stress.

Additionally, to evaluate whether these transcripts could be translated after exiting BR-bodies, we performed a series of experiments designed to distinguish between translation of pre-existing transcripts and translation of newly transcribed mRNAs. In wild-type *C. crescentus*, nutrient replenishment after the stationary phase was examined under conditions where new RNA synthesis was blocked with rifampicin. RNE-mEos3.2 fluorescence recovered substantially over 6 h following whole-cell bleaching (Fig. 4a, b), indicating that recovery does not require transcription of new mRNAs and must arise from mRNAs that existed prior to rifampicin treatment. To confirm that this recovery reflects active translation rather than delayed protein maturation, we inhibited translation with chloramphenicol, which abolished fluorescence recovery, indicating that the signal arises from newly synthesized protein and not from maturation of pre-existing fluorescent proteins.

We then asked whether BR-bodies are required for this post-stress recovery. In cells expressing RNE-ΔCTD, which are unable to form BR-bodies, fluorescence recovery for SpmX-mEos3.2 and RNE-ΔCTD-mEos3.2 was minimal following nutrient replenishment and was similar to the translation-inhibited wild-type cells (Fig. 4a, b). This result indicates that BR-bodies are required to maintain mRNAs in a translatable state during the stationary phase. Importantly, we observed a similar behavior for *spmX* and *rne* transcripts, suggesting that BR-body-mediated transcript storage and translation upon release is a general mechanism not limited to *rne*. To confirm the presence of full-length mRNA that is capable of being translated within stationary phase BR-bodies, we amplified the full-length *ctrA* mRNA by RT-PCR and found that full-length mRNA is indeed present within the BR-body (Supplementary Fig. 9c). The observed translation of released mRNA from BR-bodies suggests that BR-bodies can store functionally intact mRNAs for later translation upon stress removal.

We ultimately assessed the functional implications of stress-induced mRNA storage in BR-bodies by comparing the growth rate of *C. crescentus* cells with wild-type RNE to cells with RNE-ΔCTD after 24 h in stationary phase (Fig. 4c). Remarkably, cells with RNE-ΔCTD exhibit a 1.5-fold reduction in growth rate and a lag phase that is 3 h longer compared to the wild-type strain following nutrient replenishment. To distinguish the role of BR-body formation from potential pleiotropic effects of disrupting degradosome assembly, we analyzed recovery dynamics in an RNE-ΔDBS strain, which lacks the degradosome binding sites on RNE and therefore cannot assemble the RNA degradosome, but still forms condensates[11]. Upon nutrient replenishment, RNE-ΔDBS cells recover with kinetics comparable to wild-type, in contrast to the slow recovery observed in the RNE-ΔCTD strain (Fig. 4b,c). These results indicate that degradosome assembly is not required for the efficient exit from the stationary phase, and instead support the conclusion that the formation of BR-bodies and their ability to store essential transcripts during stress play a critical role in enabling recovery. Thus, this functional separation-of-function mutant demonstrates that the loss of condensate formation, rather than general defects in RNA metabolism, compromises recovery in the RNE-ΔCTD mutant.

Altogether, these results suggest that during stress, BR-bodies play a critical role in storing essential transcripts, which are then readily available for translation upon return to nutrient-repleted conditions, contributing to a faster transition into exponential growth. This storage mechanism circumvents the need to synthesize new transcripts, thereby facilitating the rapid program of protein production necessary for regrowth. Importantly, we observed in *Agrobacterium tumefaciens* and *Sinorhizobium meliloti* that liquid-like BR-bodies also rigidify in the stationary phase (Supplementary Fig. 16), suggesting that the material state transition to mRNA storage may be a general feature of BR-bodies.

Discussion

BR-bodies are multifunctional biomolecular condensates that orchestrate RNA decay and store RNA transcripts during stress (Fig. 4d). Under prolonged stress, BR-bodies rigidify, resulting in decreased internal dynamics, higher biomolecular density, and compaction. This transition extends the residence time of RNE within these condensates, reduces its degradation activity, and leads to an altered degradosome deficient in RhlB. Consequently, RNA transcripts within BR-bodies are stabilized under adverse conditions. Although a significant portion of RNE and mRNAs are distributed outside BR-bodies, our data indicate that BR-body-localized RNE plays the dominant role in transcript stabilization during the stationary phase.

The stabilization of mRNA within BR-bodies is a functional bacterial adaptation that allows the preservation of valuable epigenetic information during exposure to a variety of different stressors. Upon stress removal, environmental and cellular conditions shift, triggering the restoration of dynamics and disassembly of BR-bodies. This change facilitates the release of stabilized transcripts back into the cytoplasm, where they can be promptly translated to support recovery and growth. This elegant mechanism, wherein bacteria dynamically modulate the physical and biochemical properties of BR-bodies in response to environmental cues, leverages phase separation and enzyme kinetics to exert temporal and spatial control over RNA degradation and utilization. This mechanism underscores how bacteria use biomolecular condensates not just as active enzymatic reaction sites but also as adaptive tools for managing genetic resources to ensure survival and adaptation in fluctuating environments.

The bacterial aggresome is another subcellular organelle that has recently been reported to store mRNA under arsenic stress in *E. coli*[12,13,86,87]. Our results indicate that, like aggresomes, BR-bodies store mRNA transcripts during stress conditions. However, the putative mechanisms by which aggresomes and BR-bodies stabilize mRNA differ significantly from one another. Aggresomes have been proposed to protect mRNA by excluding ribonucleases, with protein surface charge playing a crucial role[87]. Aggresomes are thought to assemble through protein aggregation, and although protein chaperones are enriched within aggresome structures, the molecular trigger of their phase separation has not been uncovered[12]. However, whether aggresomes in *E. coli* might exclude RNE[88–90], the major mRNA decay nuclease, has not yet been explored. In contrast, RNE is the central scaffold necessary for BR-body formation[11], and rather than RNE being excluded from mature BR-bodies, the material properties of the BR-bodies shut off the RNase activity. Interestingly, *C. crescentus* BR-bodies have been found to enrich the aggresome marker proteins HslU, DnaK, and ClpB[43], suggesting some functional similarity to

https://doi.org/10.1038/s41467-025-65358-y

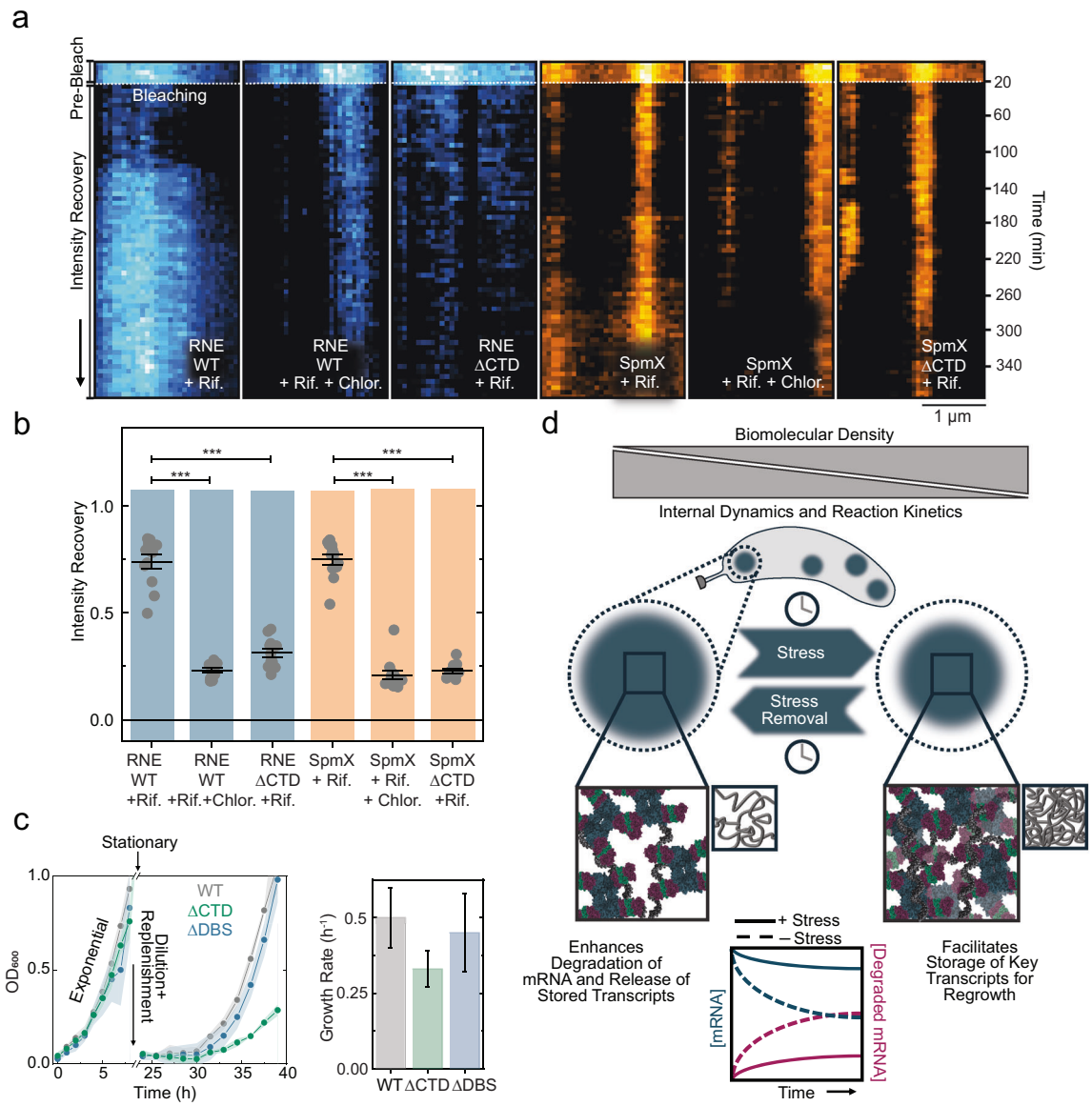

Fig. 4 | Stored mRNAs can be translated and promote rapid growth. **a** Representative kymographs of SpmX-mEos3.2 in both wild-type RNE and ΔCTD-RNE backgrounds, and of wild-type RNE and RNE-ΔCTD-mEos3.2 alone. Kymographs were generated by measuring cell fluorescence intensity along the long axis of stationary-phase *C. crescentus* cells after nutrient replenishment and inhibition of new transcript synthesis and translation with rifampicin and chloramphenicol, respectively. Similar results were obtained from three independent colony replicates. **b** Quantification of the recovery of the integrated intensity over the whole-cell area at $t = 6$ h relative to $t = 0$ h following photobleaching of the whole-cell intensity. Each dot below the distribution corresponds to the recovered intensity in one cell ($n = 12$ cells), and the error bars indicate the standard error. Two-tailed Welch's test: $p = 8.80 \times 10^{-12}$ (SpmX ΔCTD + Rif vs. SpmX + Rif), 1.03×10^{-13} (SpmX + Rif vs. SpmX + Rif + Chlor), 1.13×10^{-9} (RNE WT + Rif vs. RNE-ΔCTD + Rif), and 1.01×10^{-9} (RNE WT + Rif vs. RNE WT + Rif + Chlor). *** denotes $p < 0.001$. **c** Functional implications of mRNA storage in BR-bodies. Left: comparison of the growth rate of *C. crescentus* cells with wild-type RNE vs. cells with RNE-ΔCTD (incapable of forming BR-bodies) or RNE-ΔDBS (forms BR-bodies but cannot assemble the degradosome) when cultures are back-diluted into PYE medium after 24 h in the stationary phase. Right: growth rates following nutrient replenishment; bars indicate growth rates obtained from exponential fits to averaged growth curves ($n = 3$ replicates). Error bars indicate fitting error. Individual data points cannot be overlaid because the values are derived from averaged fits. Cells expressing RNE-ΔCTD grow more slowly following nutrient replenishment, whereas cells expressing RNE-ΔDBS grow at rates comparable to wild-type. The initial growth curves, prior to entry into the stationary phase, were initiated from back-dilutions of exponentially growing cultures. Three biological replicates were used for each condition. **d** A proposed model for how the material state of BR-bodies tunes their activity, enabling a transition from mRNA decay enhancement during growth to storage during stress.

aggresomes, yet aggresomes have a dark color in phase-contrast microscopy, whereas no such dark aggregates have been observed in *C. crescentus* at the stationary phase nor following heat shock, antibiotic treatment, or other stresses[11,35,91,92].

Despite the mechanistic data in the current study, it is still unclear how mRNA stored within BR-bodies is protected from RNE cleavage when cells transition from the stationary to the exponential phase. Potential models for future research include the possibility that *C. crescentus* possesses RNE inhibitor proteins stored within BR-bodies, similar to *E. coli* RraA and RraB[93,94]. Another hypothesis is that the RNE catalytic domain is completely denatured during rigidification and requires refolding by protein chaperones to become active again during the transition back to exponential growth.

Overall, we have determined that the function of the BR-bodies as sites of mRNA storage or decay is dictated by their material state. This model of BR-bodies underscores their role as versatile biomolecular condensates and also demonstrates how biophysical properties influence the biochemical function of condensates. The ability to modulate enzymatic activity through controlled biophysical changes within these condensates reveals a novel paradigm of gene expression regulation, which is pivotal for bacterial survival in fluctuating environments.

Methods

Plasmid and bacterial strains and construction

JS769 rne::rneΔCTD specR. 1-kB regions upstream and downstream of the RNase E NTD were PCR-amplified from *Caulobacter crescentus* NA1000 using primers Ups F and Ups R, and primers Down F and Down R. The pNTPS138 vector[95] was PCR-amplified using primers pNTPS F and pNTPS R. The DNA fragments were run on a 1% agarose gel and extracted using a GeneJet Gel Extraction kit. The vector sample was then subjected to Dpn1 treatment followed by column purification using the GeneJET PCR Purification Kit. The 1 kB insert regions were then assembled into the pNTPS138 vector via Gibson Assembly (NEB) and transformed into chemically competent *Escherichia coli* DH10B cells and plated on LB agar supplemented with kanamycin (Kan) (30 μg/mL) for selection. Colonies exhibiting resistance to Kan were screened for the presence of the insert by PCR and verified by Sanger sequencing (Genewiz).

The spectinomycin (Spec) resistance cassette was amplified from pGFP-1[95] using primers Spec F and Spec R, while the pNPTS138 RNE-ΔCTD plasmid vector was PCR-amplified using primers ΔCTD F and ΔCTD R. The Spec resistance cassette was assembled into the pNTPS138 vector via Gibson Assembly mastermix. The assembly mixture was transformed into chemically competent *E. coli* DH10B cells and plated on LB agar supplemented with Spec (50 μg/mL) and Kan for selection. Colonies exhibiting resistance to both Spec and Kan were screened for the presence of the insert by PCR and verified by Sanger sequencing (Genewiz).

For the RNE-ΔCTD strain, the purified pNTPS138 RNE-ΔCTD SpecR plasmid was introduced into NA1000 cells via tri-parental mating and plated on PYE agar plates supplemented with Nalidixic acid (Nal) + Spec + Kan (20 μg/mL Nal; 100 μg/mL Spec; 25 μg/mL Kan). The resulting *kanR*/*specR* colonies were grown in PYE without antibiotics and then counter-selected on PYE + Spec + 3% sucrose plates. SpecR and Kan-sensitive colonies were identified and screened by PCR to confirm the deletion of the CTD on the chromosome.

JS283 spmX::ms2 96× array vanA::Ms2-DM-mChy rne::rne-msfGFP specR/kanR/gentR. The *spmX::ms2* 96× arrayC-1 plasmid was generated by amplifying the last 500 bp of the *spmX* gene using the primers pspmX F and pspmX R. The resulting PCR product was column-purified, digested with KpnI and EcoRI, and ligated into pFlgC-1. Resulting *specR* colonies were screened for the spmX insert, which was validated by Sanger sequencing (Genewiz). The resulting plasmid was transformed into NA1000 and selected on PYE Spec plates. A phage lysate of strain *JS25*[35] (containing *vanA*::Ms2-DM-mChyC-2) was transduced and selected on PYE Kan/Spec plates. Finally, a phage lysate of *JS87*[35] (containing *rne*::*rne-msfGFPC*-4) was transduced, and colonies were selected on PYE Kan/Spec/Gent.

JS287 rsaA::ms2 96× array vanA::Ms2-DM-mChy rne::rne-msfGFP specR/kanR/gentR. This strain was generated in ref. 35.

JS775 rne::rne-mEos3.2C-1 SpecR. mEos3.2 was purchased as an IDT G block and digested with NcoI and NheI, then PCR-purified. The mEos3.2 insert was ligated with pYFPC-1, which was also digested with NcoI and NheI and gel-purified following restriction digestion. The resulting plasmid, pmEos3.2C-1, was transformed into DH10B cells and selected on LB Spec plates, followed by Sanger sequencing for verification. Plasmid prne-msfGFPC-1 was digested with EcoRI and NheI and gel-purified. mEos3.2 was digested from pmEos3.2C-1 with EcoRI and NheI, and the mEos3.2 insert and prneC-1 vector were ligated and selected on LB Spec plates. The resulting colonies were screened for the mEos3.2 insert, and the DNA sequence was confirmed by Sanger sequencing (Genewiz). The final prne-mEos3.2C-1 plasmid was transformed into NA1000 cells and selected on PYE Spec plates.

JS776 rne::rne-ΔCTD-mEos3.2 SpecR. The NTD of RNase E was PCR-amplified using primers HY118F and HY118R. The insert was PCR-purified and digested with NdeI and EcoRI. The pmEos3.2C-1 plasmid was used as a template to generate the mEos3.2 vector using primers HY117F and HY115R. The DNA fragments were run on a 1% agarose gel and were gel extracted using a GeneJet Gel Extraction kit. The vector sample was then subjected to Dpn1 treatment followed by column purification using the GeneJET PCR Purification Kit. The RNE NTD insert fragment was then assembled into the mEos3.2C-1 vector via Gibson Assembly (NEB) and transformed into chemically competent *E. coli* DH10B cells and plated on LB agar supplemented with Spec (50 μg/mL). The resulting SpecR colonies were grown in liquid LB + Spec (50 μg/mL) and miniprepped using the GeneJET Plasmid Miniprep Kit. The plasmid clones were screened via restriction digestion (Nde1). pRNE*ΔCTD*-mEos3.2C-1 plasmid sequencing verification was done by whole plasmid sequencing (Genewiz).

JS770 spmX::spmX-mEos3.2 specR. SpmX was PCR-amplified from NA1000 cells using primers HY116F and HY116R. The pmEos3.2C-1 plasmid was used as a template to generate the mEos3.2 vector using primers HY115F and HY115R. The DNA fragments were run on a 1% agarose gel and were gel extracted using a GeneJet Gel Extraction kit. The vector sample was then subjected to Dpn1 treatment followed by column purification using the GeneJET PCR Purification Kit. The SpmX insert fragment was then assembled into the mEos3.2C-1 vector via Gibson Assembly (NEB) and transformed into chemically competent *E. coli* DH10B cells and plated on LB agar supplemented with Spec (50 μg/mL). The resulting SpecR colonies were grown in liquid LB + Spec (50 μg/mL) and miniprepped using the GeneJET Plasmid Miniprep Kit. The plasmid clones were screened via restriction digestion (Nde1). pSpmx-mEos3.2C-1 plasmid sequencing verification was done by whole plasmid sequencing (Genewiz).

For the *spmX::spmX-mEos3.2 specR* strain, the purified pSpmx-mEos3.2C-1 plasmid was introduced into NA1000 cells via tri-parental mating and plated on PYE + Nal + Spec (20 μg/mL Nal; 100 μg/mL Spec) plates. The resulting SpecR colonies were grown in PYE + Spec (25 μg/mL Spec) liquid media.

JS804 rne::rne-ΔDBS-mEos3.2 SpecR. The CTD (*ΔDBS)* of RNase E was PCR-amplified from pRNE(*ΔDBS)C-1*[96] using primers HY120F and HY120R. The pmEos3.2C-1 plasmid was used as a template to generate the mEos3.2 vector using primers HY119F and HY119R. The DNA fragments were run on a 1% agarose gel and were gel extracted using a GeneJet Gel Extraction kit. The vector sample was then subjected to Dpn1 treatment followed by column purification using the GeneJET PCR Purification Kit. The RNE CTD (*ΔDBS)* insert fragment was then assembled into the mEos3.2C-1 vector via Gibson Assembly (NEB) and transformed into chemically competent *E. coli* DH10B cells and plated on LB agar supplemented with Spec (50 μg/mL). The resulting SpecR colonies were grown in liquid LB + Spec (50 μg/mL) and miniprepped using the GeneJET Plasmid Miniprep Kit. The plasmid clones were screened via restriction digestion (Nde1). pRNE*CTD*(*ΔDBS)*-mEos3.2C-1 plasmid sequencing verification was done by whole plasmid sequencing (Genewiz).

For the *rne::rne-ΔDBS-mEos3.2 SpecR* strain, the purified pRNE*ΔDBS*-mEos3.2C-1 plasmid was introduced into NA1000 cells via tri-parental mating and plated on PYE+ Nal + Spec (20 μg/mL Nal; 100 μg/mL Spec) plates. The resulting SpecR colonies were grown in PYE + Spec (25 μg/mL) liquid media.

JS805 hfq::tet rne::rne-mEos3.2C-1 specR/tetR. Phage lysate from strain *JS775* harboring pRNE-mEos3.2C-1 was transduced into CJW5477[97] cells and selected on PYE + Spec + Tet plates (100 μg/mL Spec; 2 μg/mL Tet). The resulting SpecR/TetR colonies were grown in PYE + Spec + Tet (25 μg/mL Spec; 1 μg/mL Tet) liquid media.

JS806 NA1000 rne::rneΔCTD Kan^R. The primer pair HY1′F and HY1′R were initially phosphorylated at their 5′ ends via T4 PNK. The T4 PNK reaction was incubated at 37 °C for 1 h. The T4 PNK enzyme was then heat-inactivated by incubating the sample at 65 °C for 20 min. The pRNE(NTD)-Apex2-FlgC-2[98] plasmid was used as a template for an inverse PCR reaction using the phosphorylated primers HY1′F and HY1′R. The DNA fragment was run on a 1% agarose gel and gel extracted using a GeneJet Gel Extraction kit. The sample was then subjected to Dpn1 treatment followed by column purification using the GeneJET PCR Purification Kit. The DNA fragment was self-ligated using T4 DNA ligase and transformed into chemically competent *E. coli* DH10B cells and plated on LB agar supplemented with Kan (50 μg/mL). The resulting KanR colonies were grown in liquid LB + Kan (30 μg/mL) and miniprepped using the GeneJET Plasmid Miniprep Kit. The plasmid clones were screened via restriction digestion (Nde1). pRNE*ΔCTD*-C-2 plasmid sequencing verification was done by whole plasmid sequencing (Genewiz).

For the *rne::rneΔCTD KanR* strain, the purified pRNE*ΔCTD*-C-2 plasmid was introduced into NA1000 cells via tri-parental mating and plated on PYE + Nal + Kan (20 μg/mL Nal; 25 μg/mL Kan) plates. The resulting KanR colonies were grown in PYE + Kan (5 μg/mL) liquid media.

JS807 NA1000 rne::rneΔCTD spmX::spmX-mEos3.2 specR Kan^R. Phage lysate from strain *JS806* harboring pRNE*ΔCTD*-C-2 was transduced into JS770 cells and selected on PYE + Spec + Kan (100 μg/mL Spec; 25 μg/mL Kan) plates. The resulting SpecR/KanR colonies were grown in PYE + Spec + Kan (25 μg/mL Spec; 5 μg/mL Kan) liquid media.

JS401 rne:rne-eYFP gentR. peYFPC-4[95] and pRNE-eYFPC-1[11] were digested with Nde1 and Kpn1. The DNA fragment was run on a 1% agarose gel and was gel extracted using a GeneJet Gel Extraction kit. The RNE-eYFP insert was ligated into the peYFPC-4 vector using T4 DNA ligase. The ligation reaction was then used to transform pRNE-eYFPC-4 into DH10B *E. coli* cells. The cells were selected on LB + Gent (30 μg/mL) plates, and the resulting GentR colonies were grown in liquid LB + Gent (15 μg/mL) and miniprepped using the GeneJET Plasmid Miniprep Kit. The plasmid clones were screened for the presence of the insert by PCR and verified by Sanger sequencing (Genewiz).

For the *rne:rne-eYFP gentR* strain, the purified pRNE-eYFPC-4 plasmid was transformed into NA1000 cells by electroporation and selected on PYE + Gent (5 μg/mL) plates. The resulting *gentR* colonies were grown in PYE + Gent (0.5 μg/mL) liquid media.

JS771 acnA::acnA-PAmChy specR. PAmCherry was PCR-amplified from our RNase E-PAmCherry[11] construct using primers HY24F and HY24R. The CFPC-1 vector[95] was PCR-amplified using primers HY23F and HY23R, removing the CFP gene. The DNA fragments were run on a 1% agarose gel and were gel extracted using a GeneJet Gel Extraction kit. The vector sample was then subjected to Dpn1 treatment followed by column purification using the GeneJET PCR Purification Kit. PAmCherry was then assembled into the vector via Gibson Assembly and transformed into DH10B *E. coli* cells and selected on LB + Spec plates. Using the GeneJET Plasmid Miniprep Kit, the SpecR colonies obtained were grown in liquid LB + Spec and miniprepped and screened via restriction digestion (Nde1). PAmCherryC-1 plasmid sequencing verification was done by Sanger sequencing (Genewiz).

Aconitase was PCR-amplified from NA1000 cells using primers HY47F and HY47R. The PAmCherryC-1 vector was PCR-amplified using primers HY48F and HY48R. The DNA fragments were run on a 1% agarose gel and were gel extracted using a GeneJet Gel Extraction kit. The vector sample was then subjected to Dpn1 treatment followed by column purification using the GeneJET PCR Purification Kit. Aconitase was then assembled into the PAmCherry vector via Gibson Assembly and transformed into DH10B *E. coli* cells and selected on LB + Spec plates. Using the GeneJET Plasmid Miniprep Kit, the *specR* colonies obtained were grown in liquid LB + Spec and miniprepped and screened via restriction digestion (Nde1). PAmCherryC-1 plasmid sequencing verification was done by Sanger sequencing (Genewiz).

To generate the NA1000 *acnA::acnA-PAmChy specR* strain, the purified aconitase-PAmCherryC-1 plasmid was mated into NA1000 cells via tri-parental mating and plated on PYE + Nal + Spec plates. The resulting *specR* colonies were grown in PYE + Spec liquid media.

JS772 acnA::acnA-PAmChy rne::rne-eYFP specR gentR. Phage lysate from strain *JS401* harboring pRNE-eYFPC-4 was transduced into *JS771* cells and selected on PYE + Spec + Gent plates (100 μg/mL Spec; 5 μg/mL Gent). The resulting SpecR/GentR colonies were grown in PYE + Spec + Gent (25 μg/mL Spec; 0.5 μg/mL Gent) liquid media.

JS773 rhlB::rhlB-PAmChy SpecR. RhlB was PCR-amplified from NA1000 cells using primers HY49F and HY49R. The PAmCherryC-1 vector was PCR-amplified using primers HY50F and HY50R. The DNA fragments were run on a 1% agarose gel and gel extracted using a GeneJet Gel Extraction kit. The vector sample was then subjected to Dpn1 treatment followed by column purification using the GeneJET PCR Purification Kit. RhlB was then assembled into the PAmCherry vector via Gibson Assembly and transformed into DH10B *E. coli* cells and selected on LB + Spec plates. Using the GeneJET Plasmid Miniprep Kit, the SpecR colonies obtained were grown in liquid LB + Spec and miniprepped and screened via restriction digestion (Nde1). PAmCherryC-1 plasmid sequencing verification was done by Sanger sequencing (Genewiz).

To generate NA1000 *rhlB::rhlB-PAmChy SpecR*, the purified rhlB-PAmCherryC-1 plasmid was mated into NA1000 cells via tri-parental mating and plated on PYE + Nal + Spec plates. The resulting SpecR colonies were grown in PYE + Spec media.

JS774 rhlB::rhlB-PAmChy rne::rne-eYFP specR gentR. Phage lysate from strain *JS401* harboring pRNE-eYFPC-4 was transduced into *JS773* cells and selected on PYE + Spec + Gent plates. The resulting SpecR/GentR colonies were grown in PYE + Spec + Gent liquid media.

JS777 ctrA::ms2 48× array kanR. The ms2 48× array repeat sequence was PCR-amplified from an IDT G block into two distinct fragments with overlapping overhangs using primers HY55F and HY55R to generate fragment 1 and primers HY56F and HY54R to generate fragment 2. The YFPC-1[95] vector was PCR-amplified using primers HY53F and HY53R, removing the YFP gene. The DNA fragments were run on a 1% agarose gel and gel extracted using a GeneJet Gel Extraction kit. The vector sample was then subjected to Dpn1 treatment followed by column purification using the GeneJET PCR Purification Kit. The ms2 48× array sequence was then cloned into the vector via Gibson Assembly (NEB) and transformed into DH10B *E. coli* cells and selected on LB + Kan plates. Using the GeneJET Plasmid Miniprep Kit, the kanR colonies obtained were grown in liquid LB + Kan and miniprepped and screened via restriction digestion (EcoR1). The ms2 48× array plasmid sequence verification was done by Sanger sequencing (Genewiz).

CtrA was PCR-amplified from NA1000 cells using primers HY63F and HY63R. The ms2 48× array vector was PCR-amplified from the ms2 48× array plasmid using primers HY64F and HY64R. The DNA fragments were run on a 1% agarose gel and were gel extracted using a GeneJet Gel Extraction kit. The vector sample was then subjected to Dpn1 treatment followed by column purification using the GeneJET PCR Purification Kit. CtrA was then assembled into the ms2 48× array vector via Gibson Assembly and transformed into DH10B *E. coli* cells and selected on LB + Kan plates. Using the GeneJET Plasmid Miniprep Kit, the KanR colonies obtained were grown in liquid LB + Kan and miniprepped and screened via restriction digestion (EcoR1). The ctrA ms2 48× array plasmid sequence verification was done by Sanger sequencing (Genewiz).

To generate the NA1000 *ctrA::ms2 48× array kanR* strain, the purified ctrA ms2 48× array plasmid was mated into NA1000 cells via tri-parental mating and plated on PYE + Nal + Kan plates. The resulting KanR colonies were grown in PYE + Kan media.

JS778 spmX::ms2 48× array kanR. SpmX was PCR-amplified from NA1000 cells using primers HY57F and HY57R. The ms2 48× array vector was PCR-amplified from the ms2 48× array plasmid using primers HY58F and HY58R. The DNA fragments were run on a 1% agarose gel and were gel extracted using a GeneJet Gel Extraction kit. The vector sample was then subjected to Dpn1 treatment followed by column purification using the GeneJET PCR Purification Kit. SpmX was then assembled into the ms2 48× array vector via Gibson Assembly and transformed into DH10B *E. coli* cells and selected on LB + Kan plates. Using the GeneJET Plasmid Miniprep Kit, the KanR colonies obtained were grown in liquid LB + Kan and miniprepped and screened via restriction digestion (EcoR1). The spmX ms2 48× array plasmid sequence verification was done by Sanger sequencing (Genewiz).

To generate the NA1000 *spmX::ms2 48× array kanR* strain, the purified spmX ms2 48× array plasmid was mated into NA1000 cells via tri-parental mating and plated on PYE + Nal + Kan plates. The resulting KanR colonies were grown in PYE + Kan media.

JS779 rsaA::ms2 48× array kanR. RsaA was PCR-amplified from NA1000 cells using primers HY61F and HY61R. The ms2 48× array vector was PCR-amplified from the ms2 48× array plasmid using primers HY62F and HY62R. The DNA fragments were run on a 1% agarose gel and were gel extracted using a GeneJet Gel Extraction kit. The vector sample was then subjected to Dpn1 treatment followed by column purification using the GeneJET PCR Purification Kit. RsaA was then assembled into the ms2 48× array vector via Gibson Assembly and transformed into DH10B *E. coli* cells and selected on LB + Kan plates. Using the GeneJET Plasmid Miniprep Kit, the KanR colonies obtained were grown in liquid LB + Kan and miniprepped and screened via restriction digestion (EcoR1). The rsaA ms2 48× array plasmid sequence verification was done by Sanger sequencing (Genewiz).

To generate the NA1000 *rsaA::ms2 48× array kanR* strain, the purified rsaA ms2 48× array plasmid was mated into NA1000 cells via tri-parental mating and plated on PYE + Nal + Kan plates. The resulting KanR colonies were grown in PYE + Kan media.

JS780 ctrA::ms2 48× array vanA::Ms2-DM-mChy rne::rne-msfGFP specR/kanR/gentR. Phage lysate from strain *JS777* harboring ctrA ms2 48× array KanR was transduced into *JS285* cells and selected on PYE + Spec + Gent + Kan plates. The resulting SpecR/GentR/KanR colonies were grown in PYE + Spec + Gent + Kan liquid media.

JS789 spmX::ms2 48× array vanA::Ms2-DM-mChy rne::rne-msfGFP specR/kanR/gentR. Phage lysate from strain *JS778* harboring spmX ms2 48× array KanR was transduced into *JS285* cells and selected on PYE + Spec + Gent + Kan plates. The resulting SpecR/GentR/KanR colonies were grown in PYE + Spec + Gent + Kan liquid media.

JS790 rsaA::ms2 48× array vanA::Ms2-DM-mChy rne::rne-msfGFP specR/kanR/gentR. Phage lysate from strain *JS779* harboring rsaA ms2 48× array KanR was transduced into *JS285* cells and selected on PYE + Spec + Gent + Kan plates. The resulting SpecR/GentR/KanR colonies were grown in PYE + Spec + Gent + Kan liquid media.

Cell growth and treatment

All *C. crescentus* strains used in this study were derived from the wild-type strain NA1000. Cultures were grown at 28 °C with shaking at 250 rpm in peptone-yeast extract (PYE) medium or M2 minimal medium supplemented with 0.2% glucose (M2G)[99]. Where necessary, antibiotics were added to the media at the following concentrations: gentamycin (0.5 µg/mL), kanamycin (5 µg/mL), spectinomycin (25 µg/mL), and streptomycin (25 µg/mL). Experiments were performed during either the exponential phase (OD_{600} ~ 0.7) or the stationary phase (24 h after reaching an OD_{600} of 1.2). For acute treatments, exponential phase cells were treated with puromycin (150 µg/mL) for 30 min, CCCP (100 µM) in DMSO for 20 min, or a combination of chloramphenicol (200 µg/mL) and CCCP, or 10% ethanol. For the combination of chloramphenicol and CCCP, the chloramphenicol was added 1 min before adding the CCCP. Stress treatments were conducted by exposing the cells to specific stress conditions for the indicated durations, followed by spotting 2 µL of culture onto a 2% (w/v) agarose pad for imaging. All imaging was conducted at 28 °C using an objective heater (Bioptechs).

Agrobacterium tumefaciens and *Sinorhizobium meliloti* were cultured in PYE medium supplemented with gentamycin (50 µg/mL) at 28 °C with shaking at 250 rpm. Experiments with these strains were conducted during the exponential phase (OD_{600} 0.5–0.7) or the stationary phase (36 h post-inoculation).

Liquid growth curves

The NA1000 and RNE-ΔCTD strains were cultured in PYE medium at 28 °C to either exponential (OD_{600} ~ 0.6) or stationary phase (24 h after OD_{600} reached 1.2). Cells were subsequently diluted in fresh PYE medium to an OD_{600} of 0.05. OD_{600} was measured approximately every hour. OD_{600} was measured in a cuvette using a Biochrom WPA CO8000 cell density meter at 600 nm. For the RNE-ΔCTD strain, Spec (25 mg/mL) was added to the initial cultures of the RNE-ΔCTD strain. Growth rates were extracted by fitting the growth curves with a single-exponential function.

Biorthogonal Non-Canonical Amino Acid Tagging (BONCAT)

BONCAT was performed on NA1000 cells across various growth phases, treated with 10% ethanol after 30 min and 2 h, and CCCP (100 µM for 20 min). Control samples included exponential phase cultures without azidohomoalanine (AHA) or with 100 µg/mL chloramphenicol. For the assay, 1.5 mL of cells were incubated with 200 µM of AHA for 30 min at 28 °C. Post-incubation, cells were washed once with 500 µL of PBS, then fixed in 100 µL of 4% formaldehyde for 30 min at 28 °C. Cells were subsequently washed once with 500 µL of PBS, then resuspended in 100 µL ice-cold 70% ethanol and incubated on ice for 30 min. After another PBS wash, cells were resuspended in 300 µL of 0.1 mM iodoacetamide and incubated at 28 °C for 30 min. Following a final wash, cells were resuspended in a freshly prepared Alkyne-Cy5 cocktail (50 µM $CuSO_4$, 250 µM tris(3-hydroxypropyltriazolylmethyl)amine (THPTA), 25 µM Alkyne-Cy5, 1 mM Aminoguanidine HCl, 2.5 mM sodium ascorbate in PBS) and incubated at room temperature for 30 min. The cocktail was chilled on ice for 10 min prior to application. After two washes in PBS, cells were resuspended in 20–200 µL PBS, depending on the pellet size, and imaged using the fluorescence channel with a 100 ms exposure time. Fluorescence intensity was calculated using the MicrobeJ[100] software tool.

Relative intracellular ATP level measurement

Intracellular ATP levels were quantified using a luciferase-based assay (BacTiter-Glo), following the manufacturer's protocol (Promega). Luminescence was measured using a microplate reader (Molecular Devices SpectraMax iD3) with white-walled luminescence 96-well plates to minimize crosstalk between wells. All cultures were adjusted to the same optical density.

mRNA half-life measurement

C. crescentus NA1000 cells were grown to exponential phase (OD_{600} ~ 0.3–0.6), early stationary phase (OD = 1.2), or late stationary phase (72 h post-OD 1.2). Additionally, JS263 cells were grown to the exponential and late stationary phase. At time zero (before rifampicin addition), 1 mL of cells was collected and immediately vortexed with 2 mL of RNAprotect Bacterial reagent. Additional 1-mL aliquots were taken at specific time intervals (1, 2, 4, 8, 16, and 32 min) after the addition of rifampicin (200 μg/mL) and treated similarly. TRIzol was pre-warmed to 65 °C. Cells in RNAprotect were pelleted by centrifugation at 6300 × *g* for 2 min, resuspended in 1 mL of pre-warmed TRIzol, and incubated at 65 °C for 10 min. Subsequently, 200 μL of chloroform was added, and the mixture was incubated at room temperature for 5 min before centrifuging at maximum speed for 10 min. The aqueous phase was transferred to a new tube, followed by an additional chloroform extraction with 500 μL. The upper aqueous phase was again collected, to which 2 μL of glycogen and 700 μL of ice-cold isopropanol were added, and samples were incubated overnight at −80 °C. The next day, samples were centrifuged at maximum speed at 4 °C for 1 h. The supernatant was discarded, and the pellet was washed with 800 μL of ice-cold 80% ethanol, followed by another centrifugation step. The supernatant was discarded, then the pellet was air-dried and resuspended in 50 μL of resuspension buffer (10 mM Tris-HCl, pH 7.0, 0.1 mM EDTA).

For RT-qPCR, a master mix was prepared containing 1× Luna Universal One-Step Reaction Mix, 1× Luna WarmStart RT Enzyme Mix, 0.4 μM each of forward and reverse primers, and milliQ water. The following primer pairs were used to test the half-lives of each these RNAs: tmRNA/*ssRA* (5′ ssRA F tccggcttcggccgaacta and 5′ ssRA R tggagccgccgggaatcg), *ctrA* (CtrA F actgatgctgaagtctgaagg and CtrA R gattgaggtcgagcaggataag), *spmX* (SpmX F ctgctgctctatgatctcatctc and SpmX R gaagttgtcgaggccgatatt), *rne* (RNE F cgcgaaatccgtgatcgt and RNE R cgcgtctcgaacactatctaatc), and 5S (5S F ccattccgaactcggtcgttaag and 5S R tggcggcgacctactct). RNA samples (100 ng/μL) were aliquoted into a 96-well plate, mixed with the master mix, and briefly centrifuged. qRT-PCR reactions were performed using a QuantStudio Real-Time PCR system. RNA decay rates were calculated by fitting a linear curve to the natural logarithm of the fraction of RNA remaining at each time point. The quantity of RNA at each time point was normalized to the amount detected in the time zero sample as 100%. The mRNA half-life was determined using linear regression of the ln (percentage of RNA remaining) at each time point of RNA extraction and converted the slope to a half-life using ($t_{1/2} = -\ln(2)/\text{slope}$).

To assess full-length mRNA levels at the stationary phase, reverse transcription reactions were performed using extracted total RNA as the template, by applying the Invitrogen first-strand cDNA synthesis technique with Superscript III. The RNA templates used were extracted from NA1000 cells from time points 0 and 16 min in both log and stationary phase. 2 pmol of *ctrA* RT FL R primer (tcaggcggcgttaacctgctc) and 1 μL of dNTP mix (10 mM each of dATP, dGTP, dCTP, and dTTP) were combined with 1 μg of total RNA. The sample was heated to 65 °C for 5 min and then incubated on ice for 1–2 min. Afterward,1 μL of DTT (0.1 M), 4 μL of 5× First-strand buffer, 1 μL of SUPERase-In RNase inhibitor (20 units/μL), and 1 μL Superscript III (200 Units/μL) were added to the mixture, and the samples were incubated at 55 °C for 60 min. The samples were heated at 70 °C for 15 min to inactivate the reaction. PCR was then performed using the resulting cDNA as a template for amplification. A 50 μL PCR reaction was conducted by adding 25 μL of Betaine (5 M), 12 μL of 5× HF-buffer, 7.5 μL of milliQ water, 3 μL of ctrA RT FL R primer (10 μM), 3 μL of ctrA RT FL F primer (10 μM) (atgcgcgtactgttgatcgagg), 1 μL dNTP mix (10 mM), 2 μL of cDNA from the reverse transcriptase reaction, and 0.5 μL of Phusion enzyme (2 Units/μL). 25 PCR cycles were performed on the log phase samples, while 30 PCR cycles were performed on the stationary phase samples. 25 μL from each PCR sample was then run on a 1% agarose gel and imaged post ethidium bromide staining.

The same experiment was repeated utilizing 5S RT FL primers (5S RT FL F gacctggtggctatgccgg; 5S RT FL R gacctggcggcgacctac) to measure the full-length mRNA levels of 5S ribosomal RNA in log and stationary phase. 10 PCR cycles were performed on both log and stationary phase samples.

Time-lapse BR-body disassembly fluorescent imaging

JS87 cells were cultured overnight in PYE + Gent medium and then inoculated into M2G medium. The cells were incubated in M2G at 28 °C for 24 h post cell reaching an OD of 1.2. 1 μL of cells was immobilized on a 1.5% (w/v) agarose pad made from fresh M2G medium and sealed with melted wax. To take the images, a Nikon Eclipse NI-E fitted with a CoolSNAP MYO-CCD camera and a 100× Oil CFI Plan Fluor (Nikon) objective was controlled using Nikon Elements software. The same field of view was imaged under the phase-contrast and GFP channels every 30 min over the span of 6 h.

Wide-field fluorescence and phase-contrast microscopy

Wide-field fluorescence and phase-contrast images were acquired with a Nikon Ti2-E motorized inverted microscope equipped with a SOLA 365 LED light source, a 100× oil immersion objective, and a Hamamatsu Orca-Flash 4.0 LTS camera. The system was controlled via NIS Elements software. Fluorescent protein fusions were imaged using specific filter sets from Chroma: mEos3.2 and YFP fusions were visualized with a YFP filter set (C-FL YFP, hard coat, high signal-to-noise ratio, zero shift, excitation: 500 ± 10 nm, emission: 535 ± 15 nm, dichroic mirror: 515 nm); GFP fusions with a GFP filter set (C-FL GFP, hard coat, high S/N, zero shift, excitation: 436 ± 10 nm, emission: 480 ± 20 nm, dichroic mirror: 455 nm); mCherry fusions with a Texas Red filter set (C-FL Texas Red, hard coat, high S/N, zero shift, excitation: 560 ± 20 nm, emission: 630 ± 37.5 nm, dichroic mirror: 585 nm); and CFP fusions with a CFP filter set (C-FL CFP, hard coat, high S/N, zero shift, excitation: 436 ± 20 nm, emission: 480 ± 40 nm, dichroic mirror: 455 nm).

Live-cell fluorescence recovery after photobleaching (FRAP)

FRAP was performed using a Nikon Ti2-E motorized inverted microscope, equipped with a SOLA 365 LED source, a 100× objective (oil immersion), and a Hamamatsu Orca-Flash 4.0 LTS camera. Control images were taken prior to bleaching, and subsequently, the regions of interest (ROIs) were bleached with a laser at 405 nm and 30% power (~15 mW). Image acquisition was performed with 300-ms integration times. More than ten different ROIs were chosen per sample. Images were analyzed with Fiji[101]: the off-cell background signal was subtracted from the bleached ROI and an unbleached ROI of the same size within the cell. The resulting intensity in the ROI was normalized such that the intensity before bleaching equals one and the first frame after bleaching equals zero.

Live-cell single-molecule fluorescence microscopy

Caulobacter crescentus cells expressing RNE-mEos3.2, RNE-YFP/Aconitase-PAmChy, and RNE-YFP/RhlB-PAmChy fusions were cultured overnight in 75 mL of PYE medium until they reached the exponential phase (OD_{600}~0.7). The following day, the cultures were diluted 1:100 into 75 mL of M2G medium and grown to an OD_{600} ~ 0.7 for imaging during the exponential phase and stress experiments, or for 24 h post-

OD_{600} ~ 1.2 for imaging during the stationary phase. The cells were immobilized on 2% (w/v) agarose pads made from spent M2G medium. To prepare the spent medium, an aliquot of the culture was centrifuged at 3500 × *g* for 8 min, and the supernatant was filtered twice through a 0.22-µm syringe filter. Imaging was performed using a wide-field Olympus IX71 inverted microscope equipped with a 100× oil immersion objective (1.40 NA). Photoconversion of mEos3.2 and PAmChy was achieved with 75- to 150-ms pulses of a 405 nm laser (Coherent Cube 405-100; 2 W/cm²), followed by imaging with a 561 nm laser (Coherent Sapphire, 561-50; 0.34 kW/cm²). For RNE-YFP/Aconitase-PAmChy and RNE-YFP/RhlB-PAmChy strains, RNE-YFP was imaged for 10 s using a 488-nm laser (Coherent Cube 488-50; 0.4 W/cm²) immediately after the 561-nm imaging to locate BR-bodies. Frames were captured at 50 Hz using a 512 × 512 Photometrics Evolve EMCCD camera.

Live-cell single-molecule data analysis

The recorded movies were analyzed using the SMALL-LABS[102] algorithm for single-molecule localization and tracking. To classify RNE-mEos3.2 trajectories between inside or outside of BR-bodies, we accounted for the dynamic and transient nature of BR-body formation, especially in exponential phase cells. Each movie was divided into consecutive 30-s submovies, reflecting the approximate lifetime of BR-bodies in exponential phase cells under our imaging conditions. For each submovie, a composite image was generated and used to segment BR-body foci using intensity-based thresholding. Only foci containing at least three single-molecule trajectories were retained for analysis. Overlapping or ambiguous foci were excluded to ensure reliable assignment. Single-molecule trajectories were then categorized based on their spatial overlap with BR-body regions: 'In' if entirely within a focus for the entire duration, 'In/Out' if overlapping with a focus for 25–99% of their duration, and 'Out' if overlapping for less than 25% of their duration. This strict classification ensures that 'In' trajectories reflect on motion within the BR-body interior and are not influenced by entry or exit events. To assess whether condensate motion could affect our measurements, we analyzed BR-body motion using trajectories matched in length to those of individual RNE molecules. This analysis showed no significant difference in BR-body mobility between exponential and stationary phases. For aconitase-PAmChy, the same trajectory classification strategy was used. In the exponential phase, aconitase-PAmChy itself served as the BR-body marker for segmentation. In the stationary phase, BR-body masks were generated by summing 10-s 488 nm channel movies collected immediately after the 561 nm imaging, allowing consistent identification and segmentation of BR-bodies under both conditions.

To characterize the diffusion of single RNE molecules within BR-bodies, we calculated the 2D apparent diffusion coefficient (D_{app}) for each trajectory by fitting the mean-squared displacement (MSD) as a function of time lag (τ) over the interval 20–100 ms. Ensemble-averaged diffusion coefficients were also obtained by fitting the MSD curve averaged across all trajectories. Given that RNE-mEos3.2 diffusion within BR-bodies during the stationary phase is nearly indistinguishable from that observed in fixed cells, indicating motion is limited by localization precision, we did not calculate the anomalous diffusion exponent α, as it is no longer informative of confinement under these conditions.

Cluster analysis

C. crescentus expressing RNase E-mEos3.2 was grown to OD_{600} ~ 0.7 for imaging during the exponential phase and stress experiments, and for 24 h after cells reached OD_{600} ~ 1.2 for imaging during the stationary phase. Prior to imaging, the cells were fixed using formaldehyde cross-linking with 1% fixation buffer, followed by a 10-min incubation at room temperature and 30 min incubation on ice, and finally washed three times with M2G. Before imaging, cells were resuspended in M2G and were subsequently spotted on 2% (w/v) agarose in M2G medium pads with Fluoresbrite carboxylate YG beads at a concentration of 5.0×10^7 beads/mL as fiducial markers. Before tracking, movies were corrected for drift. Tracking was performed using SMALL-LABS.

Oversampling, caused by including multiple localizations of the same protein that emit for more than one frame, can create false clustering. Before analyzing clustering in fixed cells, oversampling was removed with a radial and temporal filter. For each single molecule, a spatial filter with a size of $\sqrt{{\sigma_x}^2 + {\sigma_y}^2}$ was used, where σ is the localization precision (Supplementary Fig. 17)[103]. The temporal threshold was acquired by fitting the probability of finding another localization within the spatial threshold to an exponential decay and using the time constant as the threshold. To determine which class of single molecules was a cluster, Density-Based Spatial Clustering of Applications with Noise (DBSCAN)[45] was used; the constant neighborhood radius, ε, was set to 50 nm, and the minimum points was set to 20. The diameter of the clusters was calculated as the maximum span of each cluster. The number of localizations per cluster used for the determination of BR-body density and the fractions of localizations of RNE, aconitase, and RhlB correspond to the number of localizations after temporal and radial filtering identified with DBSCAN, with the parameters reported above.

To assess the recruitment of RNA degradosome components (RNase E, aconitase, and RhlB) to BR-bodies in *C. crescentus*, we combined single-molecule tracking (SMT) with whole-cell fluorescence intensity analysis. For each protein and growth phase (exponential and stationary), we calculated the fraction of single molecules localized within BR-bodies. Three biological replicates were analyzed per condition. To account for differences in total protein expression across growth phases, we normalized the fraction of BR-body-localized trajectories by the total cellular fluorescence intensity of the respective protein. These values were obtained by summing the fluorescence signal across all frames of the SMT acquisition movies for each replicate. This normalized recruitment index reflects the proportion of total cellular protein localized to BR-bodies, enabling direct comparison of BR-body enrichment between conditions.

RNE residence times in the BR body

Due to the fast photobleaching of fluorescent proteins, continuous single-molecule tracking cannot accurately determine residence time, as both dissociation and photobleaching contribute to signal loss. To overcome these factors, we performed time-lapse imaging to capture the residence behavior of RNE-mEos3.2 molecules at multiple timescales. In our time-lapse imaging, every frame was captured with a 250-ms integration time, τ_{int}, and a time delay, τ_{delay} = 300, 350, 750, or 1250 ms, was introduced between each pair of consecutive frames. An integration time of 250 ms was chosen to intentionally blur fast-diffusing RNE-mEos3.2 molecules not associated with BR-bodies, thereby enhancing the detection of slow-moving molecules likely localized within BR-bodies. To further ensure accurate assignment, we applied the same trajectory classification strategy used in the RNE-mEos3.2 mobility analysis to filter the resulting trajectories.

To measure the timescale of RNE residence inside the BR-bodies, we modeled the interaction between RNE and the BR-bodies as a simple association/dissociation reaction that has a forward reaction constant of k_{diss}^{app}. This apparent dissociation rate of RNE includes contributions from the true dissociation rate, k_{diss}, and the photobleaching rate, k_{pb}. k_{res}^{app} was obtained by plotting the $(1 - CDF)$ distribution of RNE dwell times, $\tau_{measured}$, for each of the time-lapse experiments and fitting to a single-exponential function, where the extracted rate corresponds to k_{res}^{app}. Photobleaching of mEos3.2 only occurs when laser illumination is on (i.e., only during τ_{int}) while the actual dissociation of RNE from the BR-bodies can occur at any time during the time-lapse period, $\tau_{TL} = \tau_{int} + \tau_{delay}$. These processes contribute independently to k_{diss}^{app}, and respectively produce the two terms

on the right-hand side of:

$$k_{diss}^{app}\tau_{TL} = \tau_{TL}k_{diss} + \tau_{int}k_{pb} \quad (1)$$

As shown in Eq. (1), the relationship between $k_{diss}^{app}\tau_{TL}$ and τ_{TL} is linear. Hence, the residence time, τ_{res}, was extracted from the reciprocal of the slope, k_{diss}, of the plot of $k_{diss}^{app}\tau_{TL}$ versus τ_{TL}. The linear regression also took the uncertainty of each data point from the exponential fitting into consideration and gave the final slope, k_{diss}, and its associated error.

Determination of mRNA storage with the MS2 system

Strains *JS777*, *JS778*, *JS779*, *JS780*, *JS283*, and *JS287* containing RNase E-GFP and a non-dimerizable mutant of the Ms2 coat protein fused to mCherry, along with an array of MS2-RNA hairpins fused to the 3′ end of the *rsaA*, *spmX*, *ctrA*, or *rne* genes, respectively, were grown to OD_{600}~ 0.7 for imaging during the exponential phase and stress experiments. These strains were grown for 24 h after reaching OD_{600}~1.2 for imaging during the stationary phase. The cells were immobilized on 2% (w/v) agarose: spent M2G medium pad and imaged using the system described above ("Wide-field fluorescence and phase-contrast microscopy" section), and Fluoresbrite carboxylate YG beads were added at a concentration of 5.0×10^7 beads/mL as fiducial markers. Time-lapse movies were collected using 250-ms integration times and a delay between frames of 10 and 30 s for exponential and stationary phases, respectively. After data collection, the movies were drift-corrected by using the drift path of the fiducial markers.

Colocalization between the RNE-GFP and the mRNA::*ms2*-mCherry foci was performed through thresholding. After correcting for photobleaching in both channels by implementing the exponential fitting method in ImageJ[104], Gaussian fitting was used to acquire the position of the foci in the GFP channel, and an ROI of 3 × 3 pixels (210 nm × 210 nm in our imaging setup) was used to get the intensity of the foci. The focus intensity was defined as the average intensity of the ROI. The same ROI in the same position was then applied to the mCherry channel, and the intensity was measured as in the GFP channel. An intensity threshold of 2000 counts was set to determine whether or not there was a focus at the same position in the mCherry channel. Only ROIs in the mCherry channel that contained foci colocalized with the foci in the GFP channel were considered for the analysis. Tracking was performed in foci that were colocalized in both channels. The minimum trajectory length was set to 4 frames. After tracking, the intensities of each focus in both channels were divided by the intensity of the focus at time zero (when the focus forms) to determine the intensity enhancement of each focus at each time. Recruitment of transcripts across growth phases and acute stresses was quantified using Pearson correlation coefficients (PCC). For each cell, the PCC was computed from the pixel intensities of the RNA channel and the pixel intensities of the BR-body marker channel within the segmented cell mask after background subtraction.

Translation of *rne* and *spmX* upon nutrient replenishment

Nutrients were replenished by adding fresh M2G medium to stationary phase cultures of *C. crescentus* RNE-mEos3.2 and RNE-ΔCTD-mEos3.2, while simultaneously adding rifampicin at a concentration of 75 μg/mL to inhibit transcription. Following this inhibition, the mEos3.2 fluorescence intensity was bleached using 488-nm excitation, and intensity recovery was monitored. The cells were incubated on the microscope stage with an objective heater set to 28 °C.

Fluorescence in situ hybridization (FISH)

Cells were grown, then fixed with 1% formaldehyde for 15 min at room temperature, followed by an additional 30 min on ice. The cells were harvested by centrifugation at 5500 × *g* for 4 min. The resulting cell pellets were washed twice with ice-cold 1× PBS. The cells were then pelleted again at 5500 × *g* for 4 min and washed three times with GTE buffer. Cell lysis was performed using 4000U of RNase-free lysozyme at 37 °C for 2 h. Following lysis, the cells were centrifuged, and the pellet was resuspended in 100 μL of hybridization buffer (Stellaris RNA FISH) containing 1 μL of the FISH probe (Biosearch). The control involved treating the samples with RNaseA (Thermo Fisher) before adding the FISH probe. The samples were incubated overnight at 42 °C. Post-hybridization, the cells were centrifuged and washed with 1 mL of wash buffer A at 42 °C for 30 min, followed by a wash with 1 mL of wash buffer B (Stellaris) at 42 °C for 5 min. Finally, the cells were resuspended in GTE buffer supplemented with 0.1% TritonX-100, mounted on slides using 2% agarose pads, and imaged in the wide-field fluorescence microscopy system described above ("Wide-field fluorescence and phase-contrast microscopy" section). The FISH tmRNA/*ssrA*-Cy3 probe used was 5′-CGGCGAACTCTTCAGCGAAGTTA TCGTTCGC-3′ (Integrated DNA Technologies). The probes for *ctrA*, *spmX*, and *rsaA* (Biosearch) are reported in Supplementary Table 5. The fluorophore used for *ctrA* and *spmX* was Quasar 570, and Quasar 670 was used for *rsaA*.

Protein purification

An overnight culture of *E. coli* BL21(DE3) transformed with the pVN030 plasmid encoding MBP-RNE CTD (461-898 aa) was reinoculated into 1.5 L of LB medium containing 30 μg/mL kanamycin and grown at 37 °C with shaking at 200 rpm until the OD_{600} reached approximately 0.6. Expression of MBP-RNE CTD was induced by adding 0.5 mM IPTG, followed by incubation at 37 °C with shaking at 140 rpm for 3 h. Cells were harvested by centrifugation at 2500 × *g* for 15 min and resuspended in 20 mL of lysis buffer (20 mM Tris, pH 7.4, 500 mM NaCl, 10% glycerol, 10 mM imidazole, 1 mM PMSF, 2 tablets protease inhibitor cocktail, and 10 μg/mL DNase I). The cells were lysed using sonication at 4 °C, over 18 cycles of 5 s on and 20 s off. The lysate was centrifuged at 19,200 × *g* for 45 min at 4 °C, and the supernatant was loaded onto pre-equilibrated Ni-NTA resin to bind the 6× His-MBP-RNE (461-868). The resin-bound protein was washed with 5 column volumes each of low salt buffer (20 mM Tris, pH 7.4, 150 mM NaCl, 5% glycerol, 10 mM imidazole) and high salt buffer (20 mM Tris, pH 7.4, 1000 mM NaCl, 5% glycerol, 10 mM imidazole), before elution with elution buffer (20 mM Tris, pH 7.4, 150 mM NaCl, 5% glycerol, 250 mM imidazole). The protein was concentrated using an Amicon concentrator with a 30 kDa cutoff and dialyzed against 20 mM Tris, pH 7.4, 150 mM NaCl buffer. The concentrated protein was stored at −80 °C.

Full-length GFP-RNE, encoded by the pVN059 plasmid, was purified using the same protocol as previously described[71]. The Ni-NTA affinity-purified GFP-RNE full-length was concentrated using an Amicon concentrator with a 50 kDa cutoff and further purified by size exclusion chromatography on an S200 Sephadex column to remove contaminant proteins. The final protein was eluted in 20 mM Tris, pH 7.4, 150 mM NaCl, 2% glycerol, concentrated to ~10 mg/mL, and stored at −80 °C.

TEV protease was purified using a similar protocol, except the plasmid conferred ampicillin resistance. The Ni-NTA affinity-purified TEV protease was concentrated using an Amicon concentrator with a 10 kDa cutoff and further purified by size exclusion chromatography on an S200 Sephadex column in 20 mM Tris, pH 7.4, 150 mM NaCl, and 5% glycerol. The protein was stored at −80 °C in 1 mg/mL aliquots.

In vitro transcription of RNase E 5′ UTR

The plasmid containing RNase E 5′ UTR (pVN053) was linearized using Nhe1 restriction enzyme, which served as the template for in vitro transcription (IVT). The IVT reaction mixture contained 2.7 mg of linearized plasmid, 21 μg homemade T7 RNA polymerase, 2.5 mM NTPs, 1× reaction buffer (50 mM Tris-Cl, pH 7.4, 15 mM $MgCl_2$, 5 mM DTT, 2 mM spermidine), 0.01 U/μL PPase in a total volume of 1000 μL, and the reaction was carried out at 37 °C for 4 h. The transcribed RNA loaded onto 7% Urea gel was extracted using phenol-chloroform and

ethanol precipitation methods. The precipitated RNA was resuspended in nuclease-free water.

pCp Cy5 labeling of RNase E 5′ UTR

In vitro transcribed RNase E 5′ UTR (4.5 μM) was incubated with 33 μM of pCp Cy5 in a total reaction volume of 100 μL consisting of 50 units of T4 RNA ligase 1, 1 mM ATP, 10% DMSO, 1× T4 RNA ligase reaction buffer for 16 h at 16 °C. Following the reaction, T4 RNA ligase 1 was heat-inactivated at 65 °C for 15 min, and the reaction mixture was subjected to a phenol-chloroform extraction to remove the enzyme. The unincorporated pCp Cy5 was removed by passing the labeled RNA through a Sephadex G-50 column and elution in nuclease-free water.

In vitro condensate assay and RNA degradation in the condensates

20 μM of MBP-RNase E CTD (461-868) was treated with 1 μM of TEV protease at room temperature in 20 mM Tris pH 7.4, and 100 mM NaCl in a total reaction volume of 10 μL for 45 min to cleave off the MBP tag from RNase E CTD. The formation of RNase E CTD condensates was verified by microscopy, followed by the addition of 1 μM GFP RNase E full-length and 0.5 μM RNase E 5′ UTR Cy5. After 10 min, the recruitment of GFP RNase E full-length and RNase E 5′ UTR into RNase E CTD condensates was verified using a Nikon Eclipse NI-E with CoolSNAP MYO-CCD camera and 100× Oil CFI Plan Fluor (Nikon) objective under GFP and Cy5 channels with 50 ms exposures. The condensates were incubated for 30 min, 4 h, or 8 h in separate tubes, followed by the addition of 200 μM MgCl2 to each tube to stimulate GFP RNase E full-length endonucleolytic activity. At the end of each time point, 2 μL from the reaction was quenched with 8 μL quench buffer (20 mM Tris pH 7.4, 50 mM EDTA, 0.1% SDS) and 3 μL of quenched reaction was mixed with 7 μL loading buffer (95% formamide, 10 mM EDTA, 0.1% SDS, 0.025% bromophenol blue, 0.025% xylene cyanol), boiled at 90 °C for 2 min before loaded onto 7% urea PAGE. The gel was run in a Biorad Mini-PROTEAN tetra cell system at 190 V for 45 min. The gel was stained with 1× SYBR gold for 20 min and scanned using a Thermo Fisher iBright imaging system.

RNE CTD (461-868) generation and Cy5 labeling

6×-His-MBP-RNase E CTD and TEV protease were incubated at a molar ratio of 20:1 in 20 mM Tris (pH 7.4) and 150 mM NaCl for 16 h at 4 °C with gentle rocking. The cleavage of MBP was confirmed using SDS-PAGE. The reaction mixture was then loaded onto pre-equilibrated Ni-NTA resin and incubated for 5 min to bind the 6× His-MBP to the resin. The unbound RNase E CTD was collected, and its purity was assessed via SDS-PAGE. RNase E CTD was concentrated using an Amicon concentrator with a 10-kDa cutoff. Cy5 labeling was performed following previously described protocols[43]. Briefly, Cy5 NHS ester dye dissolved in DMSO was incubated with RNase E CTD in an equal molar ratio in 0.1 M sodium bicarbonate buffer (pH 8.5) at room temperature for 4 h. Excess dye was removed by dialysis against 20 mM Tris (pH 7.4) and 150 mM NaCl using a dialysis cassette with a 3-kDa cutoff.

In vitro FRAP of RNE CTD condensates

To form RNE CTD Cy5 condensates, 20 μM RNE CTD Cy5 was incubated in 20 mM Tris (pH 7.4) and 100 mM NaCl at room temperature for 20 min, in a total reaction volume of 10 μL. Following this incubation, 1 μM GFP-RNE full-length and 0.5 μM RNE 5′ UTR were added to the condensates. The mixtures were incubated for 30 min, 4 h, and 8 h, respectively. At the end of each incubation period, 6 μL of the reaction mixture was placed onto a homemade well slide, covered with a coverslip, and FRAP was performed using a Zeiss LSM 800 microscope. The diameters of the bleached and reference areas within the condensates were set to 2 μm. The resulting intensity in the ROI was normalized such that the intensity before bleaching equals one and the first frame after bleaching equals zero.

Statistical analysis of distributions

$p > 0.05$ was considered not significant. $^{*}p \leq 0.05$, $^{**}p \leq 0.01$, $^{***}p \leq 0.001$ were considered significant using a two-tailed Welch's *t*-test.

Reporting summary

Further information on research design is available in the Nature Portfolio Reporting Summary linked to this article.

Data availability

All data generated and analyzed during this study are included in this published article and its Supplementary Information files. Source data are provided with this paper.

Code availability

Data processing and analysis scripts for this study were written in MATLAB and Python. The code used for this study is available on GitHub. Image analysis scripts: https://github.com/BiteenMatlab/bacterial_condensates (https://doi.org/10.5281/zenodo.10806033); and SMALL-LABS algorithm package: https://github.com/BiteenMatlab/SMALL-LABS.

References

1. Banani, S. F., Lee, H. O., Hyman, A. A. & Rosen, M. K. Biomolecular condensates: organizers of cellular biochemistry. *Nat. Rev. Mol. Cell Biol.* **18**, 285–298 (2017).
2. Boeynaems, S. et al. Protein phase separation: a new phase in cell biology. *Trends Cell Biol.* **28**, 420–435 (2018).
3. Yoo, H., Triandafillou, C. & Drummond, D. A. Cellular sensing by phase separation: Using the process, not just the products. *J. Biol. Chem.* **294**, 7151–7159 (2019).
4. Ditlev, J. A., Case, L. B. & Rosen, M. K. Who's in and who's out—compositional control of biomolecular condensates. *J. Mol. Biol.* **430**, 4666–4684 (2018).
5. Nakamura, H., DeRose, R. & Inoue, T. Harnessing biomolecular condensates in living cells. *J. Biochem.* **166**, 13–27 (2019).
6. Aguzzi, A. & Altmeyer, M. Phase separation: linking cellular compartmentalization to disease. *Trends Cell Biol.* **26**, 547–558 (2016).
7. Ramaswami, M., Taylor, J. P. & Parker, R. Altered ribostasis: RNA-protein granules in degenerative disorders. *Cell* **154**, 727–736 (2013).
8. Zhu, L. et al. Controlling the material properties and rRNA processing function of the nucleolus using light. *Proc. Natl. Acad. Sci. USA* **116**, 17330–17335 (2019).
9. Dorone, Y. et al. A prion-like protein regulator of seed germination undergoes hydration-dependent phase separation. *Cell* **184**, 4284–4298.e27 (2021).
10. Bose, M., Lampe, M., Mahamid, J. & Ephrussi, A. Liquid-to-solid phase transition of *oskar* ribonucleoprotein granules is essential for their function in *Drosophila* embryonic development. *Cell* **185**, 1308–1324.e23 (2022).
11. Al-Husini, N., Tomares, D. T., Bitar, O., Childers, W. S. & Schrader, J. M. α-Proteobacterial RNA degradosomes assemble liquid-liquid phase-separated RNP bodies. *Mol. Cell* **71**, 1027–1039.e14 (2018).
12. Pu, Y. et al. ATP-dependent dynamic protein aggregation regulates bacterial dormancy depth critical for antibiotic tolerance. *Mol. Cell* **73**, 143–156.e4 (2019).
13. Jin, X. et al. Membraneless organelles formed by liquid-liquid phase separation increase bacterial fitness. *Sci. Adv.* **7**, eabh2929 (2021).
14. Heinkel, F. et al. Phase separation and clustering of an ABC transporter in Mycobacterium tuberculosis. *Proc. Natl. Acad. Sci. USA* **116**, 16326–16331 (2019).
15. MacCready, J. S., Basalla, J. L. & Vecchiarelli, A. G. Origin and evolution of carboxysome positioning systems in cyanobacteria. *Mol. Biol. Evol.* **37**, 1434–1451 (2020).

16. McQuail, J., Carpousis, A. J. & Wigneshweraraj, S. The association between Hfq and RNase E in long-term nitrogen-starved Escherichia coli. *Mol. Microbiol.* **117**, 54–66 (2022).
17. Azaldegui, C. A., Vecchiarelli, A. G. & Biteen, J. S. The emergence of phase separation as an organizing principle in bacteria. *Biophys. J.* **120**, 1123–1138 (2021).
18. Saurabh, S. et al. ATP-responsive biomolecular condensates tune bacterial kinase signaling. *Sci. Adv.* **8**, eabm6570 (2022).
19. Lasker, K. et al. Selective sequestration of signalling proteins in a membraneless organelle reinforces the spatial regulation of asymmetry in Caulobacter crescentus. *Nat. Microbiol.* **5**, 418–429 (2020).
20. Surovtsev, I. V. & Jacobs-Wagner, C. Subcellular organization: a critical feature of bacterial cell replication. *Cell* **172**, 1271–1293 (2018).
21. Treuner-Lange, A. & Søgaard-Andersen, L. Regulation of cell polarity in bacteria. *J. Cell Biol.* **206**, 7–17 (2014).
22. Hammarlöf, D. L., Bergman, J. M., Garmendia, E. & Hughes, D. Turnover of mRNAs is one of the essential functions of RNase E. *Mol. Microbiol.* **98**, 34–45 (2015).
23. Ono, M. & Kuwano, M. A conditional lethal mutation in an *Escherichia coli* strain with a longer chemical lifetime of messenger RNA. *J. Mol. Biol.* **129**, 343–357 (1979).
24. Kedersha, N. et al. Stress granules and processing bodies are dynamically linked sites of mRNP remodeling. *J. Cell Biol.* **169**, 871–884 (2005).
25. Hubstenberger, A. et al. P-Body Purification Reveals the Condensation of Repressed mRNA Regulons. *Mol. Cell* **68**, 144–157.e5 (2017).
26. Youn, J.-Y. et al. Properties of stress granule and p-body proteomes. *Mol. Cell* **76**, 286–294 (2019).
27. Rathnayaka-Mudiyanselage, I., Nandana, V. & Schrader, J. Proteomic composition of eukaryotic and bacterial RNA decay condensates suggests convergent evolution. *Curr. Opin. Microbiol.* **79**, 102467 (2024).
28. Brengues, M., Teixeira, D. & Parker, R. Movement of eukaryotic mRNAs between polysomes and cytoplasmic processing bodies. *Science* **310**, 486–489 (2005).
29. Sheth, U. & Parker, R. Decapping and decay of messenger RNA occur in cytoplasmic processing bodies. *Science* **300**, 805–808 (2003).
30. Xing, W., Muhlrad, D., Parker, R. & Rosen, M. K. A quantitative inventory of yeast P body proteins reveals principles of composition and specificity. *eLife* **9**, e56525 (2020).
31. Blake, L. A., Watkins, L., Liu, Y., Inoue, T. & Wu, B. A rapid inducible RNA decay system reveals fast mRNA decay in P-bodies. *Nat. Commun.* **15**, 2720 (2024).
32. Wheeler, J. R., Matheny, T., Jain, S., Abrisch, R. & Parker, R. Distinct stages in stress granule assembly and disassembly. *eLife* **5**, e18413 (2016).
33. Moon, S. L. et al. Multicolour single-molecule tracking of mRNA interactions with RNP granules. *Nat. Cell Biol.* **21**, 162–168 (2019).
34. Mateju, D. et al. An aberrant phase transition of stress granules triggered by misfolded protein and prevented by chaperone function. *EMBO J.* **36**, 1669–1687 (2017).
35. Al-Husini, N. et al. BR-bodies provide selectively permeable condensates that stimulate mRNA decay and prevent release of decay intermediates. *Mol. Cell* **78**, 670–682.e8 (2020).
36. Chen, H., Shiroguchi, K., Ge, H. & Xie, X. S. Genome-wide study of mRNA degradation and transcript elongation in Escherichia coli. *Mol. Syst. Biol.* **11**, 781 (2015).
37. Barnett, T. C., Bugrysheva, J. V. & Scott, J. R. Role of mRNA stability in growth phase regulation of gene expression in the group A streptococcus. *J. Bacteriol.* **189**, 1866–1873 (2007).
38. Hambraeus, G., von Wachenfeldt, C. & Hederstedt, L. Genome-wide survey of mRNA half-lives in Bacillus subtilis identifies extremely stable mRNAs. *Mol. Genet. Genomics* **269**, 706–714 (2003).
39. Dressaire, C. et al. PNPase is involved in the coordination of mRNA degradation and expression in stationary phase cells of Escherichia coli. *BMC Genomics* **19**, 848 (2018).
40. Esquerré, T. et al. Dual role of transcription and transcript stability in the regulation of gene expression in Escherichia coli cells cultured on glucose at different growth rates. *Nucleic Acids Res.* **42**, 2460–2472 (2014).
41. Morrison, J. M., Anderson, K. L., Beenken, K. E., Smeltzer, M. S. & Dunman, K. M. The staphylococcal accessory regulator, SarA, is an RNA-binding protein that modulates the mRNA turnover properties of late-exponential and stationary phase Staphylococcus aureus cells. *Front. Cell. Infect. Microbiol.* **2**, 26 (2012).
42. Zhang, M. et al. Rational design of true monomeric and bright photoactivatable fluorescent proteins. *Nat. Methods* **9**, 727–729 (2012).
43. Nandana, V. et al. The BR-body proteome contains a complex network of protein-protein and protein-RNA interactions. *Cell Rep.* **42**, 113229 (2023).
44. Hardwick, S. W., Chan, V. S. Y., Broadhurst, R. W. & Luisi, B. F. An RNA degradosome assembly in Caulobacter crescentus. *Nucleic Acids Res.* **39**, 1449–1459 (2011).
45. Ester, M., Kriegel, H.-P., Sander, J. & Xu, X. A density-based algorithm for discovering clusters in large spatial databases with noise. In *Proc. Second International Conference on Knowledge Discovery and Data Mining* 226–231 (AAAI Press, 1996).
46. Parry, B. R. et al. The bacterial cytoplasm has glass-like properties and is fluidized by metabolic activity. *Cell* **156**, 183–194 (2014).
47. Kroschwald, S. et al. Promiscuous interactions and protein disaggregases determine the material state of stress-inducible RNP granules. *eLife* **4**, e06807 (2015).
48. Kroschwald, S., Maharana, S. & Simon, A. Hexanediol: a chemical probe to investigate the material properties of membrane-less compartments. *Matters*. https://doi.org/10.19185/matters.201702000010 (2017).
49. Lin, Y. et al. Toxic PR poly-dipeptides encoded by the C9orf72 repeat expansion target LC domain polymers. *Cell* **167**, 789–802.e12 (2016).
50. Hondele, M. et al. DEAD-box ATPases are global regulators of phase-separated organelles. *Nature* **573**, 144–148 (2019).
51. Deng, Y., Beahm, D. R., Ionov, S. & Sarpeshkar, R. Measuring and modeling energy and power consumption in living microbial cells with a synthetic ATP reporter. *BMC Biol.* **19**, 101 (2021).
52. Weber, S. C., Spakowitz, A. J. & Theriot, J. A. Nonthermal ATP-dependent fluctuations contribute to the in vivo motion of chromosomal loci. *Proc. Natl. Acad. Sci. USA* **109**, 7338–7343 (2012).
53. Russell, R., Jarmoskaite, I. & Lambowitz, A. M. Toward a molecular understanding of RNA remodeling by DEAD-box proteins. *RNA Biol.* **10**, 44–55 (2013).
54. Li, X.-Z., Plésiat, P. & Nikaido, H. The challenge of efflux-mediated antibiotic resistance in Gram-negative bacteria. *Clin. Microbiol. Rev.* **28**, 337–418 (2015).
55. Nathans, D. Puromycin inhibition of protein synthesis: incorporation of puromycin into peptide chains. *Proc. Natl. Acad. Sci. USA* **51**, 585–592 (1964).
56. Oh, E. et al. Selective ribosome profiling reveals the cotranslational chaperone action of trigger factor in vivo. *Cell* **147**, 1295–1308 (2011).
57. Pontes, M. H., Sevostyanova, A. & Groisman, E. A. When too much ATP is bad for protein synthesis. *J. Mol. Biol.* **427**, 2586–2594 (2015).

58. Stouthamer, A. H. A theoretical study on the amount of ATP required for synthesis of microbial cell material. *Antonie Van Leeuwenhoek* **39**, 545–565 (1973).
59. Patel, A. et al. A liquid-to-solid phase transition of the ALS protein FUS accelerated by disease mutation. *Cell* **162**, 1066–1077 (2015).
60. Molliex, A. et al. Phase separation by low complexity domains promotes stress granule assembly and drives pathological fibrillization. *Cell* **163**, 123–133 (2015).
61. Zhang, H. et al. RNA controls PolyQ protein phase transitions. *Mol. Cell* **60**, 220–230 (2015).
62. Lin, Y., Protter, D. S. W., Rosen, M. K. & Parker, R. Formation and maturation of phase-separated liquid droplets by RNA-binding proteins. *Mol. Cell* **60**, 208–219 (2015).
63. Xiang, S. et al. The LC domain of hnRNPA2 adopts similar conformations in hydrogel polymers, liquid-like droplets, and nuclei. *Cell* **163**, 829–839 (2015).
64. Watanabe, H. Viscoelasticity and dynamics of entangled polymers. *Prog. Polym. Sci.* **24**, 1253–1403 (1999).
65. Halfmann, R. A glass menagerie of low complexity sequences. *Curr. Opin. Struct. Biol.* **38**, 18–25 (2016).
66. Mittag, T. & Pappu, R. V. A conceptual framework for understanding phase separation and addressing open questions and challenges. *Mol. Cell* **82**, 2201–2214 (2022).
67. Boke, E. et al. Amyloid-like self-assembly of a cellular compartment. *Cell* **166**, 637–650 (2016).
68. Linsenmeier, M. et al. Dynamic arrest and aging of biomolecular condensates are modulated by low-complexity domains, RNA and biochemical activity. *Nat. Commun.* **13**, 3030 (2022).
69. Bertrand, E. et al. Localization of ASH1 mRNA particles in living yeast. *Mol. Cell* **2**, 437–445 (1998).
70. Tutucci, E. et al. An improved MS2 system for accurate reporting of the mRNA life cycle. *Nat. Methods* **15**, 81–89 (2018).
71. Nandana, V., Al-Husini, N., Vaishnav, A., Dilrangi, K. H. & Schrader, J. M. Caulobacter crescentus RNase E condensation contributes to autoregulation and fitness. *Mol. Biol. Cell* **35**, ar104 (2024).
72. Awram, P. & Smit, J. The Caulobacter crescentus paracrystalline S-layer protein is secreted by an ABC transporter (type I) secretion apparatus. *J. Bacteriol.* **180**, 3062–3069 (1998).
73. Wheeler, R. T. & Shapiro, L. Differential localization of two histidine kinases controlling bacterial cell differentiation. *Mol. Cell* **4**, 683–694 (1999).
74. Radhakrishnan, S. K., Thanbichler, M. & Viollier, P. H. The dynamic interplay between a cell fate determinant and a lysozyme homolog drives the asymmetric division cycle of Caulobacter crescentus. *Genes Dev.* **22**, 212–225 (2008).
75. Ryan, K. R., Judd, E. M. & Shapiro, L. The CtrA response regulator essential for *Caulobacter crescentus* cell-cycle progression requires a bipartite degradation signal for temporally controlled proteolysis. *J. Mol. Biol.* **324**, 443–455 (2002).
76. Wortinger, M., Sackett, M. J. & Brun, Y. V. CtrA mediates a DNA replication checkpoint that prevents cell division in Caulobacter crescentus. *EMBO J.* **19**, 4503–4512 (2000).
77. Laub, M. T., Chen, S. L., Shapiro, L. & McAdams, H. H. Genes directly controlled by CtrA, a master regulator of the Caulobacter cell cycle. *Proc. Natl. Acad. Sci. USA* **99**, 4632–4637 (2002).
78. Laub, M. T., McAdams, H. H., Feldblyum, T., Fraser, C. M. & Shapiro, L. Global analysis of the genetic network controlling a bacterial cell cycle. *Science* **290**, 2144–2148 (2000).
79. Quon, K. C., Marczynski, G. T. & Shapiro, L. Cell cycle control by an essential bacterial two-component signal transduction protein. *Cell* **84**, 83–93 (1996).
80. LeCuyer, K. A., Behlen, L. S. & Uhlenbeck, O. C. Mutants of the Bacteriophage MS2 coat protein that alter its cooperative binding to RNA. *Biochemistry* **34**, 10600–10606 (1995).
81. Garcia, J. F. & Parker, R. MS2 coat proteins bound to yeast mRNAs block 5′ to 3′ degradation and trap mRNA decay products: implications for the localization of mRNAs by MS2-MCP system. *RNA* **21**, 1393–1395 (2015).
82. Heinrich, S., Sidler, C. L., Azzalin, C. M. & Weis, K. Stem–loop RNA labeling can affect nuclear and cytoplasmic mRNA processing. *RNA* **23**, 134–141 (2017).
83. Garcia, J. F. & Parker, R. Ubiquitous accumulation of 3′ mRNA decay fragments in Saccharomyces cerevisiae mRNAs with chromosomally integrated MS2 arrays. *RNA* **22**, 657 (2016).
84. Guan, J. et al. HP-bodies – ancestral condensates that regulate RNA turnover and protein translation in bacteria. Preprint at *bioRxiv* https://doi.org/10.1101/2025.02.06.636932 (2025)
85. Goldberger, O., Szoke, T., Nussbaum-Shochat, A. & Amster-Choder, O. Heterotypic phase separation of Hfq is linked to its roles as an RNA chaperone. *Cell Rep.* **41**, 111881 (2022).
86. Bollen, C. et al. Composition and liquid-to-solid maturation of protein aggregates contribute to bacterial dormancy development and recovery. *Nat. Commun.* **16**, 1046 (2025).
87. Pei, L. et al. Aggresomes protect mRNA under stress in Escherichia coli. *Nat. Microbiol.* **10**, 2323–2337 (2025).
88. Mudd, E. A., Krisch, H. M. & Higgins, C. F. RNase E, an endoribonuclease, has a general role in the chemical decay of Escherichia coli mRNA: evidence that rne and ams are the same genetic locus. *Mol. Microbiol.* **4**, 2127–2135 (1990).
89. Górna, M. W., Carpousis, A. J. & Luisi, B. F. From conformational chaos to robust regulation: the structure and function of the multienzyme RNA degradosome. *Q. Rev. Biophys.* **45**, 105–145 (2012).
90. Bandyra, K. J., Bouvier, M., Carpousis, A. J. & Luisi, B. F. The social fabric of the RNA degradosome. *Biochim. Biophys. Acta* **1829**, 514–522 (2013).
91. Schramm, F. D., Schroeder, K., Alvelid, J., Testa, I. & Jonas, K. Growth-driven displacement of protein aggregates along the cell length ensures partitioning to both daughter cells in Caulobacter crescentus. *Mol. Microbiol.* **111**, 1430–1448 (2019).
92. Wortinger, M. A., Quardokus, E. M. & Brun, Y. V. Morphological adaptation and inhibition of cell division during stationary phase in Caulobacter crescentus. *Mol. Microbiol.* **29**, 963–973 (1998).
93. Lee, K. et al. RraA: a protein inhibitor of RNase E activity that globally modulates RNA abundance in E. coli. *Cell* **114**, 623–634 (2003).
94. Górna, M. W. et al. The regulatory protein RraA modulates RNA-binding and helicase activities of the E. coli RNA degradosome. *RNA* **16**, 553–562 (2010).
95. Thanbichler, M., Iniesta, A. A. & Shapiro, L. A comprehensive set of plasmids for vanillate- and xylose-inducible gene expression in Caulobacter crescentus. *Nucleic Acids Res.* **35**, e137 (2007).
96. Passos, C. et al. BR-bodies facilitate adaptive responses and survival during copper stress in Caulobacter crescentus. *J. Biol. Chem.* **301**, 110648 (2025).
97. Irnov, I. et al. Crosstalk between the tricarboxylic acid cycle and peptidoglycan synthesis in Caulobacter crescentus through the homeostatic control of α-ketoglutarate. *PLOS Genet.* **13**, e1006978 (2017).
98. Yassine, H. et al. APEX2 proximity labeling of RNA in bacteria. *Cell Rep. Methods* **5**, 101206 (2025).
99. Schrader, J. M. & Shapiro, L. Synchronization of Caulobacter crescentus for investigation of the bacterial cell cycle. *J. Vis. Exp.* https://doi.org/10.3791/52633 (2015).
100. Ducret, A., Quardokus, E. M. & Brun, Y. V. MicrobeJ, a tool for high throughput bacterial cell detection and quantitative analysis. *Nat. Microbiol.* **1**, 1–7 (2016).
101. Schindelin, J. et al. Fiji: an open-source platform for biological-image analysis. *Nat. Methods* **9**, 676–682 (2012).

102. Isaacoff, B. P., Li, Y., Lee, S. A. & Biteen, J. S. SMALL-LABS: measuring single-molecule intensity and position in obscuring backgrounds. *Biophys. J.* **116**, 975–982 (2019).
103. Endesfelder, U., Malkusch, S., Fricke, F. & Heilemann, M. A simple method to estimate the average localization precision of a single-molecule localization microscopy experiment. *Histochem. Cell Biol.* **141**, 629–638 (2014).
104. Miura, K. Bleach correction ImageJ plugin for compensating the photobleaching of time-lapse sequences. Preprint at https://doi.org/10.12688/f1000research.27171.1 (2020).

Acknowledgements

The authors acknowledge the support of NIH grant R35GM124733 to J.M.S., NIH T32GM142519-03 to HY., and NIH grants R01GM143182 and R01GM144731 to J.S.B. The authors thank Dr. Anthony Vecchiarelli for generously providing access to his wide-field fluorescence microscope. Thanks to Dr. Tamara Hendrickson and the WSU Department of Chemistry for lab space and equipment after the Schrader lab was destroyed in a fire.

Author contributions

L.A.O.-R. designed, performed, and analyzed experiments (all live-cell single-molecule and ensemble fluorescence imaging, FRAP, FISH, growth curves, and ATP level measurements), interpreted results, and wrote the manuscript. H.Y. designed, performed, and analyzed experiments (strain construction, qRT-PCR, and BONCAT) and interpreted results. V.N., A.H., and Y.Z. designed, performed, and analyzed experiments (all in vitro reconstitution and in vitro FRAP experiments) and interpreted results. C.A.A. analyzed experiments (developed a script to isolate trajectories inside the condensates) and contributed to writing the revised manuscript. J.C. analyzed experiments (cluster analysis). J.M.S. provided expertise in the design and construction of the strains, interpreted results, and wrote the manuscript. J.S.B. provided expertise in the design of live-cell imaging experiments, designed experiments, interpreted results, and wrote the manuscript.

Competing interests

The authors declare no competing interests.

Additional information

Supplementary information The online version contains supplementary material available at https://doi.org/10.1038/s41467-025-65358-y.

Correspondence and requests for materials should be addressed to Jared M. Schrader or Julie S. Biteen.

Peer review information *Nature Communications* thanks the anonymous reviewers for their contribution to the peer review of this work. A peer review file is available.